

Superoxide intermediate in the oxygen reduction on a zinc hydroxide model corrosion product

Accepted Manuscript: This article has been accepted for publication and undergone full peer review but has not been through the copyediting, typesetting, pagination, and proofreading process, which may lead to differences between this version and the Version of Record.

Cite as: J. Chem. Phys. (in press) (2022); <https://doi.org/10.1063/5.0130076>

Submitted: 09 October 2022 • Accepted: 20 November 2022 • Accepted Manuscript Online: 21 November 2022

 Simantini Nayak,  P. Ulrich Biedermann and  Andreas Erbe



View Online



Export Citation



CrossMark

ARTICLES YOU MAY BE INTERESTED IN

[Essential Collective Dynamics Analysis Reveals Nonlocal Interactions of Alpha-Synuclein₃₈₋₉₅ Monomers with Fibrillar Seeds](#)

The Journal of Chemical Physics (2022); <https://doi.org/10.1063/5.0116032>

[Gaussian-Based Quasiparticle Self-Consistent GW for Periodic Systems](#)

The Journal of Chemical Physics (2022); <https://doi.org/10.1063/5.0125756>

[One Experiment Makes a Direct Comparison of Structural Recovery with Equilibrium Relaxation](#)

The Journal of Chemical Physics (2022); <https://doi.org/10.1063/5.0131342>

[Learn More](#)

The Journal of Chemical Physics **Special Topics** Open for Submissions

Superoxide intermediate in the oxygen reduction on a zinc hydroxide model corrosion product

Simantini Nayak,^{1,2} P. Ulrich Biedermann,¹ and Andreas Erbe^{1,3}

¹*Max-Planck-Institut für Eisenforschung GmbH, Max-Planck-Str. 1, 40237 Düsseldorf, Germany*

²*Department of Materials Chemistry, CSIR-Institute of Minerals and Materials Technology, Bhubaneswar, 751013, India*

³*Department of Materials Science and Engineering, NTNU, Norwegian University of Science and Technology, 7491 Trondheim, Norway*

(*Electronic mail: orr-zno@the-passivists.org)

(Dated: 4 November 2022)

The inhibition of the electrochemical oxygen reduction reaction (ORR) by zinc corrosion products plays an important role in the corrosion protection of galvanized steel. Hence, the electrocatalytic mechanism of the ORR on electrodeposited zinc hydroxide based model corrosion products was investigated by in situ and operando attenuated total reflection infrared (ATR-IR) spectroscopy, supplemented by density functional theory (DFT) calculations. Model corrosion products containing flake-like crystalline $\text{Zn}_5(\text{NO}_3)_2(\text{OH})_8$ were cathodically electrodeposited on germanium(100) electrodes from a zinc nitrate precursor electrolyte. Substantial amounts of the films are non-crystalline, and its surface predominantly consists of zinc oxide and hydroxide species, as evidenced by x-ray photoelectron spectroscopy (XPS). ATR-IR spectra show a peak at 1180 cm^{-1} during cathodic currents in O_2 -saturated NaClO_4 solution. This peak is assigned to a surface-bound superoxide, the only ORR intermediate detected. Absorbance from the intermediate increases with increasing cathodic current, indicating an increase in surface concentration of superoxide intermediates at larger ORR current densities. The zinc hydroxide ages in the experiments, most likely by a transformation into zinc oxide, consistent with the observed decrease of absorbance over time of the OH bending mode of zinc hydroxide at 1380 cm^{-1} . This aging is a time-dependent chemical process, implying that pure chemical aging is important in actual corrosion products also. DFT calculations of adsorbed superoxide yield a Zn-O bond length similar to the bond length in Zn-O, thus enhanced superoxide interaction with undercoordinated tetrahedral Zn^{2+} sites on the surface. Thus, such active sites catalyze the first reduction step in the ORR.

I. INTRODUCTION

The electrochemical oxygen reduction reaction (ORR), $\text{O}_2 + 4\text{H}^+ + 4\text{e}^- \longrightarrow 2\text{H}_2\text{O}$, is an important electron transfer reaction. Amongst others, it is often rate determining in corrosion processes, metal air batteries, or fuel cells.¹ While the ORR on noble metals has been extensively studied, its mechanism on practically important oxides is much less investigated. The practical importance stems from the fact that many metals are covered with an oxide layer under ORR-relevant conditions. For example, on chromium oxide, electrocatalytic activity towards ORR has been suggested in a computational study to depend strongly on doping with other metals.² The presence of Zn^{2+} and especially Mg^{2+} modifies significantly the ORR activity on iron oxides, which is important for corrosion inhibition at cut edges.³ Because of the tremendous importance of zinc and zinc alloys in corrosion protection as galvanizing coatings,⁴ this work shall look deeper into the mechanism of the ORR on (hydr)oxide based model corrosion products of zinc. To that end, we shall use electrodeposited zinc (hydr)oxide experimentally to mimic (hydr)oxide layers on zinc.

Zinc passivated by zinc oxide shows a significantly slower ORR compared to actively corroding zinc.⁵ In general, the ORR activity of an oxide-covered zinc surface strongly depends on the nature of the formed oxidation product,^{6,7} also for zinc alloy based metallic coatings.⁸ Differences can be related to the band structure and defect density of the oxide,^{9,10} which for zinc oxide strongly depends on preparation history.¹¹⁻¹³ Special inhibitors modify the defect structure in the zinc oxide on metallic zinc such that the oxide becomes similar to an intrinsic semiconductor.¹⁴ The deposition of nanocrystalline ZnO on hot-dip galvanized steel decreased the ORR activity of the surface.¹⁵ ORR on oxide covered zinc is enhanced by illumination,¹⁶ which may also be related to convection effects.¹⁷ Additional alloy elements in the metallic coatings generate oxides with decreased ORR activity compared to pure zinc.^{7,18} A well studied example is Mg in Zn-(Al)-Mg.^{7,8,19-21} The alkalisation accompanying ORR has been hypothesized to lead to the growth of ZnO nanostructures on zinc, which in turn affect corrosion and ORR kinetics.²² For TiO_2 it is known that even single atom doping can significantly enhance ORR activity.²³

ORR kinetics plays a special role in underpaint corrosion, where the cathodic delamination is usually the fastest mechanism on zinc based surfaces, including galvanized steel.²⁴⁻²⁶ On pure zinc, the confinement in combination with the relatively fast ORR rate can lead

to a depletion of water and an effective stop of ORR.^{27,28} Also for polymer coated surfaces, ORR rates strongly depend on the nature of the oxides on the surfaces;²⁹ the same is true for uncoated zinc.⁵⁻⁷ Ion release from ion exchange pigments can also inhibit ORR and thus delamination.³⁰ Thus, appropriate pretreatment will inhibit ORR activity on the surfaces at the same time as it enhances coating adhesion.³¹⁻³⁵ Conductive polymer coatings can lead to the formation of highly insulating ZnO at the interface, inhibiting cathodic delamination.^{36,37} ORR intermediates are discussed to play a crucial role in the deadhesion of organic coatings.^{28,33,38} As an alternative, OH⁻ as final ORR product can participate in interfacial degradation.^{31,33} The fact that corrosion inhibitors released from polymer coatings,³⁹ or built into the oxide layer,⁴⁰ can stop delamination may also be related to the inhibition of ORR kinetics.

ZnO on zinc is also an attractive system for generating “reactive oxygen species” (ROS) that can be used for degradation of pollutants, either through photocatalysis,⁴¹ or by what is likely a corrosion process.⁴² ROS generation can be enhanced by plasmonic structures,⁴³ or carbon structures,⁴⁴ in contact with ZnO.

Mechanistically, ORR on electrodeposited ZnO showed much less peroxide production in alkaline KCl than Pt.⁴⁵ On the other hand, a number of earlier studies showed the presence of peroxide in the ORR on zinc by rotating ring disc electrode (RRDE) experiments under many conditions.^{38,46,47} The corrosion product layer in alkaline solution, which participates in the ORR, was found to be semi-metallic;^{11,46} defects in the solid participate in the reduction reaction.⁴⁶ The ORR mechanism on zinc is potential dependent; at potentials near the open circuit potential, where the zinc is hydroxide covered, peroxide is the dominating product.^{47,48} A coupling of ORR with perchlorate adsorption was found at neutral pH.⁴⁹

While the kinetics has been well characterized, and products have been detected by RRDE, there is no in situ and operando study of the ORR mechanism on the electrode surfaces, which serves as the main motivation for this work. Model corrosion products of zinc hydroxide and zinc oxide containing layers have been electrodeposited on germanium Ge(100) internal reflection elements for use in multiple internal reflection attenuated total reflection (ATR) infrared (IR) spectroscopy. This work extends previous studies of the ORR intermediates on germanium,^{50,51} and on nanoparticles on germanium.⁵² The detection of reaction intermediates, which are present potentially only in trace level concentrations is facilitated by the use of multiple reflections in ATR-IR spectroscopy. The electrodeposited

layers have been characterized by scanning electron microscopy (SEM) with energy dispersive x-ray microanalysis (EDX), atomic force microscopy (AFM) and grazing incidence x-ray diffraction (GI-XRD); their surfaces were analyzed by x-ray photoelectron spectroscopy (XPS). As the core aspect of this work, Ge(100) substrates with model corrosion products were used to trace intermediates of the oxygen reduction by in situ and operando ATR-IR spectroscopy coupled to electrochemical experiments. Similar approaches have recently been used for model studies of the metal/polymer interface.^{53,54} To complement the experimental work, density functional theory (DFT) calculations of important ORR intermediates bound to ZnO surfaces have been carried out using a cluster model including solvation effects. For the computations, ZnO was selected as substrate because of the known atomistic structure and well studied interface with aqueous solutions. The ZnO/water interface was represented by ZnO/(10 $\bar{1}$ 0) or (0001) crystal facets covered with water molecules. The non-polar (10 $\bar{1}$ 0) facet is the most abundant ZnO crystal facet in humid environment.⁵⁵⁻⁵⁷ The zinc-terminated polar facet (0001) was included to assess the impact of different adsorption environments.

II. MATERIALS AND METHODS

A. Chemicals

All chemicals used in this work are reagent grade and used without further purification. Deionized ultrapure water (ELGA LC134, PURELAB Plus) with specific conductivity 18 $\mu\text{S cm}^{-1}$ was used for all the experiments. The PTFE ATR-IR cells and other glasswares were cleaned in piranha solution (3:1 mixture of 96% H_2SO_4 and 30% H_2O_2) and with deionized ultrapure water before each experiment. For deposition of zinc model corrosion products, electrochemical deposition from 1 M aqueous $\text{Zn}(\text{NO}_3)_2$ precursor electrolyte (pH 4.4) was chosen. For the ORR study, 0.1 M NaClO_4 at pH 10.5 was chosen as the electrolyte.

B. Preparation of internal reflection elements for ATR-IR spectroscopy

N-doped Ge(100) crystals (Universitywafers.com) with a specific resistivity of 10-40 $\Omega \text{ cm}$ and roughness $\leq 10 \text{ \AA}$ were used for the deposition of zinc hydroxide based corrosion products. ATR crystals were cut from respective double sided polished wafers of a size 52 mm \times 20 mm \times 0.5 mm. A special homemade set-up, made up of PTFE, was used to polish

the short edges of the crystals at an angle of 30° (resulting in an angle of incidence of 60°) with different polishing grade sandpapers, 400, 600 and 1000 followed by $6\ \mu\text{m}$, $3\ \mu\text{m}$ and $1\ \mu\text{m}$ of diamond polishing on MD-Mol polishing cloths (Struers). Scotch tapes were used on both sides of the crystal before polishing to prevent scratching during polishing. The chosen crystal geometry with a thin, long crystal leads to an intense interaction of the light with the species close to the surface. The polished crystals were cleaned with neutral Extran lab detergent (VWR) for 1 h followed by rinsing with ultrapure water several times, and leaving them in 2-propanol for 1 h. The crystals were subsequently rinsed with excessive amounts of ultrapure water and dried under an N_2 stream prior to each experiments. Further electrochemical experiments were carried out in the spectroelectrochemical cell. The absence of $-\text{CH}$ stretching modes during the IR spectra was used as an indication of clean ATR substrates.

C. Deposition of zinc (hydr)oxide containing model corrosion products

Model corrosion products were deposited via electrodeposition from 1 M aqueous $\text{Zn}(\text{NO}_3)_2$ precursor electrolyte (pH 4.4), based on a procedure reported in the literature.⁵⁸ The electrodeposition is based on cathodic currents leading to pH changes near the surface, which initiate precipitation of the model corrosion products. Deposition was attempted at two different pH values, at pH 4.4 and pH 2. At pH = 2 (zinc nitrate acidified with nitric acid), no deposition was observed on the Ge(100) surface. At pH = 4.4, the original pH of the $\text{Zn}(\text{NO}_3)_2$ solution, deposition was carried out in potentiostatic mode at $E = -1.19\ \text{V}$ vs. standard hydrogen electrode (SHE) under Ar atmosphere and continuous stirring for 10 s, 5 min, 10 min and 20 min. The surface was covered completely (as judged visually and by SEM) for the samples coated for 10 min and 20 min. The procedure was optimised in the in situ ATR-IR cell; ex situ characterization was performed on ATR prisms that were not used in in situ experiments with the exception of the SEM imaging after one full experimental cycle.

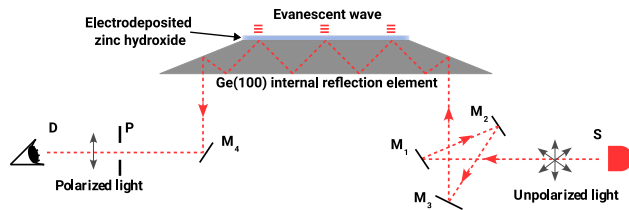


FIG. 1: Schematic view of the optical configuration in the ATR-IR experiments used here.

Light from the source S is directed via different mirrors (M) into the the germanium internal reflection element onto which model corrosion products have been deposited. An evanescent wave is generated into the electrolyte (not shown), probing changes near the surface. After exiting the internal reflection element, the light is directed via a fourth mirror through a polarizer P onto the detector D.

D. In situ electrochemical ATR-IR measurements

Fig. 1 shows the optical configuration of the setup used here. ATR-IR spectra were measured using a Biorad FTS 3000 Fourier transform IR spectrometer equipped with a middle band mercury cadmium telluride (MCT) detector. The in situ electrochemical cell has been described in detail in previous works.^{50,51} Spectra were recorded in s- and p-polarization co-adding 500 scans with a spectral resolution of 4 cm^{-1} . IR spectra are displayed as absorbance defined as

$$A = -\log_{10} \left(\frac{I_s}{I_0} \right) \quad (1)$$

where I_s and I_0 represent the light intensity of the sample- and reference spectrum, respectively. In this study, two IR spectra of the Ge(100) substrates with air as background were measured first, which were later used for the water vapor subtraction. At pH = 4.4, the pH of 1 M aqueous $\text{Zn}(\text{NO}_3)_2$ solution, deposition of zinc hydroxide layers was carried out in potentiostatic mode at $E = -1.19\text{ V}$ vs. SHE under Ar atmosphere in the spectro-electrochemical cell. After deposition, the electrolyte was changed to 0.1 M NaClO_4 at pH 10.5 for the ORR study. All spectra were recorded under potentiostatic polarization in chronoamperometry mode in potential steps of 100 mV. Voltammograms are dominated by cathodic currents (interpreted as ORR; see Results) in the region -0.3 V to -0.8 V . Accordingly, the potential window for ATR-IR measurements was chosen from -0.09 V to -0.79 V . Based on the experiences with germanium electrochemistry in similar electrolytes,^{50,59} there is a very low germanium dissolution rate at the starting potentials, from which polarisation proceeded

in negative direction. Absorbance spectra were obtained by using the spectra measured at the initial potential of +0.01 V as reference. All electrode potentials reported in this work are reported with reference to SHE. Residual contributions from atmospheric water vapor to the ATR-IR spectra were subtracted initially to exclude misinterpretations. All the ATR-IR spectra were baseline corrected. Spectra are included in the associated dataset.⁶⁰

E. Characterization of deposited layers

For the morphological characterization of deposited layers on Ge(100), a scanning electron microscope of type Leo 1550 VP Gemini (Carl Zeiss) was used. An EDX spectrometer, Oxford Instruments Model 7426, was used to determine the elemental composition of the deposited layer on the Ge surface. An atomic force microscope (Digital Instruments DIMENSION 3100 Model D3100S-1) was used to obtain the topographic information of model corrosion products. For the analysis of the AFM images the WSxM software was used.⁶¹ GI-XRD was performed using a Bruker-AXS D8 with a Cu-K α source ($\lambda=1.54 \text{ \AA}$). For the analysis of the XRD data, the Diffraction Plus database JCPDE was used. XPS was performed on a Physical Electronics PHI small spot scanning ESCA Quantum 2000 system with a Mg-K α source. Important characterisation data is included in the associated dataset.⁶⁰

F. Computations

For the calculation of vibrational modes of adsorbed ORR intermediates, small model structures of ZnO were constructed representing the essential features at the electrochemical interface. These features include the adsorption site on the solid/liquid interface and solvation effects by the surrounding water. ZnO was chosen because of (i) the abundance of literature, (ii) the fact that data on well characterized surfaces is available in the literature, and (iii) the presence of the essential chemical features perceived important for this study. For realistic models of the prepared model corrosion products in this work, a much more comprehensive background study would have been necessary. As substrate, the ZnO surface was represented by a small prismatic ZnO crystal with Wurzite structure. The triangular polar facets were passivated by a half monolayer of hydrogen atoms on the oxygen terminated facet and by a half monolayer of OH-groups on the zinc terminated facet.⁶² This

atomic structure yields a closed shell electronic structure of the crystal without partially filled surface bands.

For adsorption on the $\text{ZnO}(10\bar{1}0)$ facet, the model crystal consisted of four double layers of 10 Zn and O atoms each. For the (0001) facet two double layers of 10 Zn and O atoms were used. The ORR intermediates were adsorbed on one of the three $\text{ZnO}(10\bar{1}0)$ side facets or the (0001) facet, binding to a zinc atom close to the centre of the respective facet. The remaining zinc atoms of this facet adsorb one water molecule each in case of the $\text{ZnO}(10\bar{1}0)$ or either one of the passivating OH groups or a water molecule in case of the (0001) facet, simulating a ZnO/water interface.^{55,62,63}

The adsorbed water molecules form a network of hydrogen bonds with oxygen atoms of the surface, neighboring water molecules and the ORR intermediates. In our previous work,⁵¹ it was found that a two-layer solvation model is required to compute frequencies of species in water. This solvation model includes one explicit water molecule for each H-bonding site to include hydrogen bonding effects and embedding in a dielectric environment for the polarizing long-range electrostatics. Therefore, additional water molecules were added for each hydrogen bonding site on the ORR intermediates that is not coordinated by one of the water molecules adsorbed on neighboring surface sites. For each lone pair, a H-bond donating water molecule was added, and for each OH-group an accepting water molecule. The additional water molecules, not adsorbed on the surface, were held in a position approximating a tetrahedral coordination of the oxygen atoms of the intermediates by angle and dihedral constraints. The length of the hydrogen bond and all O-H distances and the bond angle of the water molecule were optimized. The entire atomistic model complex was embedded in a polarisable continuum to simulate the dielectric shielding and polarization by the surrounding water.

In view of the relatively large model structures, the computationally efficient generalized gradient approximation density functional BP86^{64,65} was selected and the def2-TZVP basis set.⁶⁶ The COSMO continuum solvation model was used,^{67,68} with parameters for water: $\epsilon = 78.36$, $r_{\text{solv}} = 1.30$ and $r_{\text{find}} = 1.333$. The calculations were carried out using the Turbomole program Version 6.6.⁶⁹ The structures were fully optimized with the exception of constraints on the bond angle and dihedral angle imposing the approximately tetrahedral position of the additional solvating water molecules that are not adsorbed on the ZnO cluster. For the vibrational frequencies of the adsorbed oxygen reduction intermediates, numerical

central second derivatives were calculated. Only displacements of the ORR intermediate and of the zinc and oxygen atoms at the adsorption sites were considered. No frequency scaling was applied. Optimized structures, vibrational spectra, and visualization of characteristic vibrational modes are included in the associated dataset.⁶⁰

III. RESULTS

A. Surface characterization of deposited layers

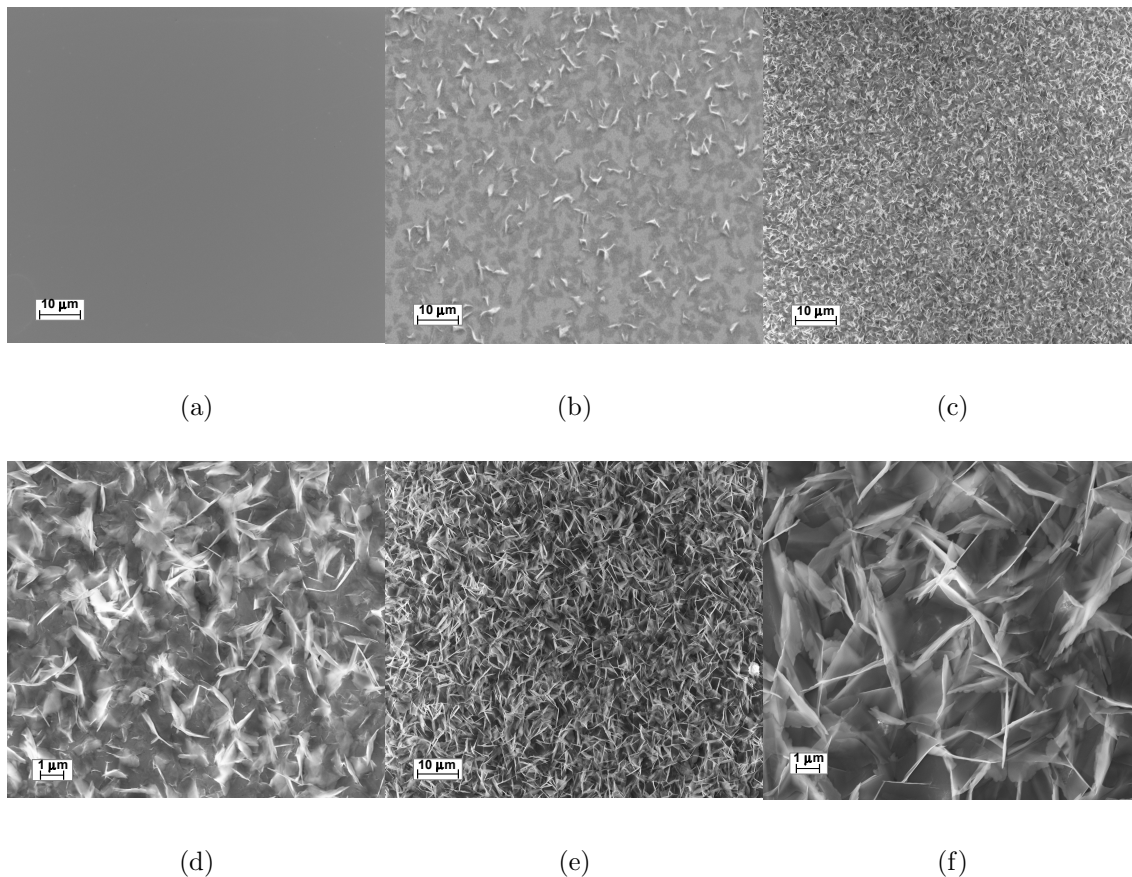


FIG. 2: SEM images of deposited films on a Ge(100) substrate; (a) bare Ge(100) substrate, (b) deposited for $t = 5$ min, (c) and (d) for $t = 10$ min, (e) and (f) for $t = 20$ min.

Fig. 2 shows examples of SEM images for deposited films obtained after different deposition times. SEM images show that some elongated features start to grow on the Ge substrate after 5 min of electrodeposition (Fig. 2b). The whole Ge surface was covered by

these elongated structures after 10 min. The potential was applied for 20 min in order to fill possible remaining gaps on the Ge substrate. EDX analysis after 20 min deposition time shows the presence of Zn, O and Ge (Fig. 3).

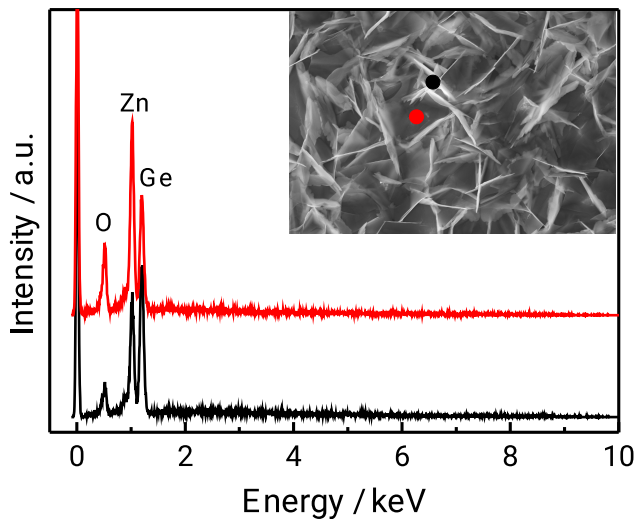


FIG. 3: EDX analysis (10 keV incidence energy) of deposited films on Ge substrate. The inset shows the SEM image for the 20 min deposited ZnO sample as shown in Fig. 2f.

As the deposition has resulted in a thin, flake-like film on the substrate, pores in the film will likely exist, which could reach the substrate. Such pores would also likely be present in real corrosion products. AFM measurements were carried out to measure the roughness of the deposited ZnO thin film (Fig. 4). The deposited film is not smooth and the root-mean-square roughness was found to be around 550 nm.

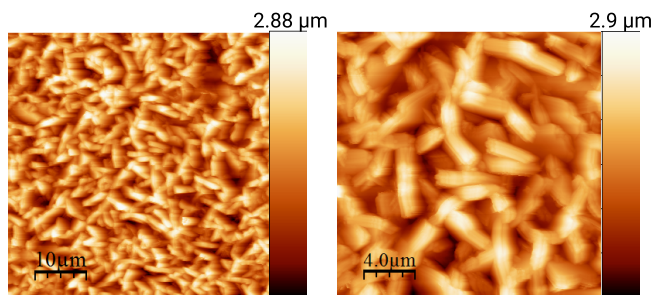


FIG. 4: AFM images of the deposited films with two different magnifications.

GI-XRD analysis was carried out for the film with 20 min deposition time in order to characterize the phases present in the sample. Fig. 5 shows the XRD pattern of the model corrosion product film. All the crystalline peaks observed matched $\text{Zn}_5(\text{NO}_3)_2(\text{OH})_8$.⁷⁰ Thus,

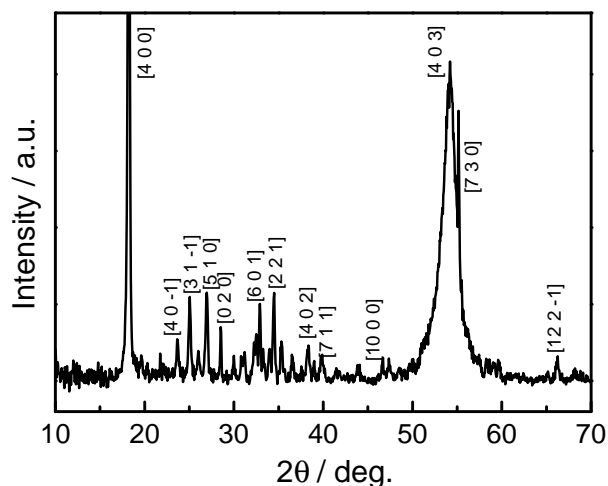


FIG. 5: GI-XRD analysis of deposited thin film on Ge substrate. All peaks can be assigned to $\text{Zn}_5(\text{NO}_3)_2(\text{OH})_8$; the assignment of the diffraction peaks is given in the figure.

this crystalline phase has formed during the electrochemically triggered deposition. No diffraction peaks were detected originating from crystalline ZnO or $\text{Zn}(\text{OH})_2$ in the XRD measurement. The sample was not annealed at elevated temperatures after deposition, and hydroxide corrosion products may be strongly disordered. Disorder explains the relatively broad peaks. Deposited oxide and hydroxide is likely mostly amorphous in nature.^{4,11,71}

XPS analysis was carried out for films deposited for 20 min on Ge. Fig. 6 shows the XPS scans for O, Zn and C core level peaks of the deposited film. The high resolution XPS scan of the C 1s region shows two peaks. The first peak at 285.2 eV is assigned to aliphatic carbon, and the second at 289.1 eV to carbonate species.⁷¹ Both of these peaks could originate from typical contaminants due to atmospheric exposure. The O 1s region shows a peak at 531.5 eV. A peak at 532 eV has been assigned to chemisorbed oxygen, dissociated oxygen or hydroxide.⁷² A peak at 530.9 eV was assigned to the presence of ZnO and at 532.3 eV of $\text{Zn}(\text{OH})_2$.⁷¹ Thus, the peak at 531.5 eV could potentially originate from the hydroxide in $\text{Zn}_5(\text{NO}_3)_2(\text{OH})_8$ or $\text{Zn}(\text{OH})_2$.⁷² The Zn $2p_{3/2}$ region shows a peak at 1022 eV, which can be attributed to Zn^{II} .⁷³ While it is quite difficult to distinguish between Zn^0 with a binding energy of 1021.8 eV,⁷⁴ and Zn^{II} with a binding energy of 1022.5,⁷⁵ or 1021.8 eV,⁷⁴ there is no reason to consider reduction to substantial amounts of metallic zinc under the conditions used here, as the optical properties in the IR exclude the presence of metallic species on the surface. The Zn $2p_{1/2}$ peak was not measured here; because of the large spin-orbit-splitting of Zn, this peak is significantly shifted compared to the Zn $2p_{3/2}$ peak. No peak for N 1s

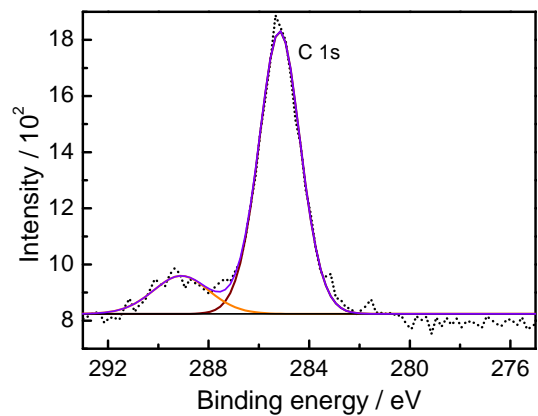
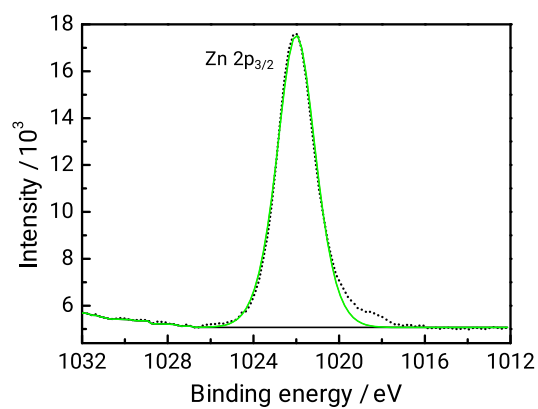
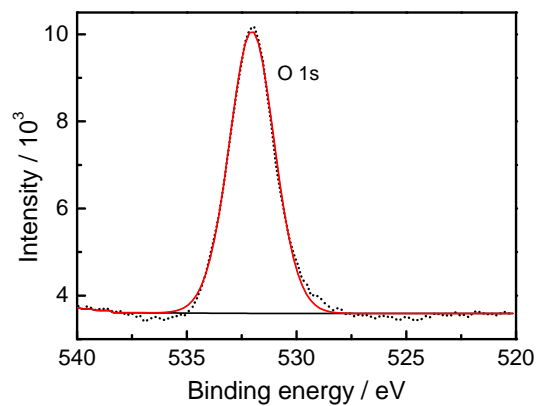


FIG. 6: XPS of deposited film, (a) O 1s region, (b) Zn $2p_{3/2}$ peak, (c) C 1s peak. \cdots : experimental result; $—$: fit.

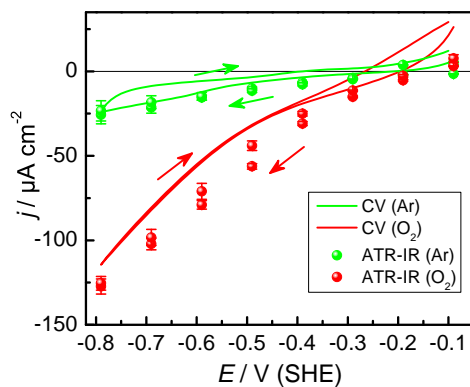
is detected during survey scans, indicating the absence of NO_3^- or any other impurities containing N on the surface.

XRD shows that the only crystalline phase in the region near the surface is $\text{Zn}_5(\text{NO}_3)_2(\text{OH})_8$, a nitrate-containing zinc hydroxide phase. N is not detected in EDX or XPS. Absence in EDX may be caused by limited energy resolution of the EDX detector and the proximity of the small N signal to the large O signal. A substantial non-crystalline fraction of the film may also contribute, as it would not contribute to crystal diffraction in XRD. The absence of N in XPS shows that the surface of the films consist predominantly of zinc oxide and hydroxide species. We employ these films here as models for the complex corrosion products of zinc.⁴

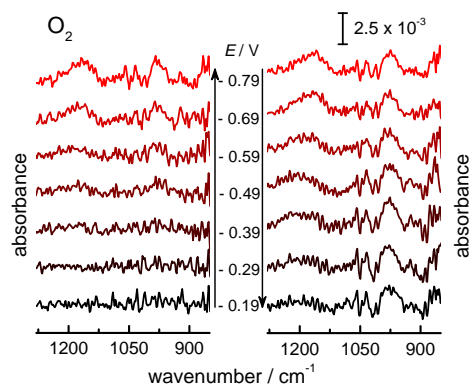
B. In situ electrochemical results and ATR-IR spectra

Fig. 7a shows typical cyclic voltammograms (CVs) at scan speeds of 50 mV/s on deposited model corrosion products in Ar and O_2 saturated 0.1 M NaClO_4 at pH 10.5. In Ar saturated solution, H_2 evolution was observed below -0.4 V. In O_2 saturated solution, an oxidation peak at -0.2 V was observed, which could be caused by re-oxidation of H_2 , though the absence of this peak in the absence of O_2 points to other effects. An alternative explanation could be reoxidation of defects in the oxide that form as part of the catalytic cycle during ORR. At negative potentials (-0.3 V to -0.8 V), ORR was observed, where it dominates over the H_2 evolution — assuming that the increased current in O_2 is caused by a pure ORR current. Fig. 7b and c show series of ATR-IR spectra recorded in p-polarization in the ORR potential window in the presence and absence of O_2 , respectively. For comparison with the CVs, the average current densities recorded during the ATR measurement are shown as circles in Fig. 7a. Compared to the current densities observed on pure Ge(100) substrates reported before,⁵⁰ the current densities on the zinc (hydr)oxide covered surface are approximately twice as high. Consequently, the results from this study can be interpreted as related to the ORR on the model corrosion products, not on the substrate.

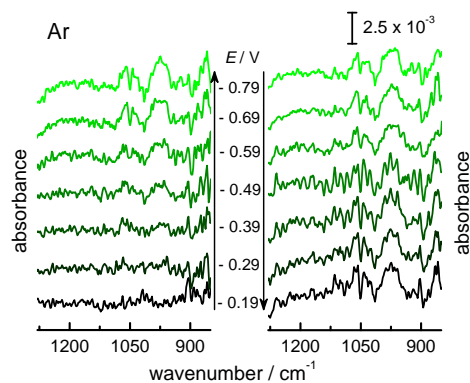
An absorption peak at 1180 cm^{-1} was observed in presence of O_2 . Its absorbance is increasing while stepping the potential negative and decreasing in the subsequent positive potential steps. Absence of the peak in the Ar purged solution clearly indicate a relation to the ORR. On the other hand, a broad absorption peak was observed at $970\text{-}980\text{ cm}^{-1}$ in



(a)



(b)



(c)

FIG. 7: (a) Lines: CV (50 mV/s) in 0.1 M NaClO₄ at pH 10.5 on zinc hydroxide model corrosion products in O₂ (—) and Ar (—) atmosphere. Arrows indicate the scan direction. Circles: Average currents during ATR-IR experiments in O₂ (●) and Ar (●) atmosphere. ATR-IR spectra in 0.1 M NaClO₄ at pH 10.5 on zinc hydroxide model corrosion products in (b) O₂ and (c) Ar atmosphere for p-polarization in the direction of decreasing potentials (left) and increasing potentials (right). Background spectrum: initial spectrum at +0.01 V.

O_2 saturated as well as in Ar purged solution. Its absorbance increases while stepping the potential negative and keeps increasing in the subsequent positive potential steps. Therefore, its growth is most likely related to aging processes in the surfaces, not to ORR. Two more peaks with absorbance continuously increasing with time were observed at 1050 cm^{-1} and 1025 cm^{-1} in the presence and absence of O_2 . Furthermore, a negative sharp peak was observed at 1380 cm^{-1} in both Ar and O_2 saturated solution (Fig. 8). In addition, 3 shoulder peaks were observed at 1325 cm^{-1} , 1396 cm^{-1} and 1440 cm^{-1} . The (negative) absorbance of these peaks was found to increase with time (rather than potential) as shown in Fig. 8.

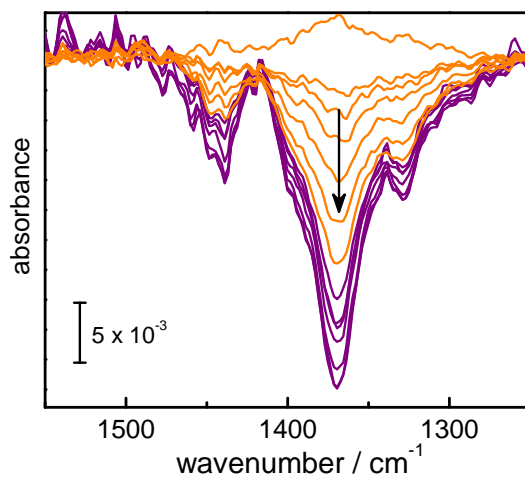
Surface morphology changes in the course of the experiment are obvious when comparing an SEM image recorded after negative polarisation in the presence of O_2 (Fig. 9) to those before experiments (Fig. 2). Larger agglomerates have formed, while the flakes of the continuous film became smaller.

C. DFT calculations

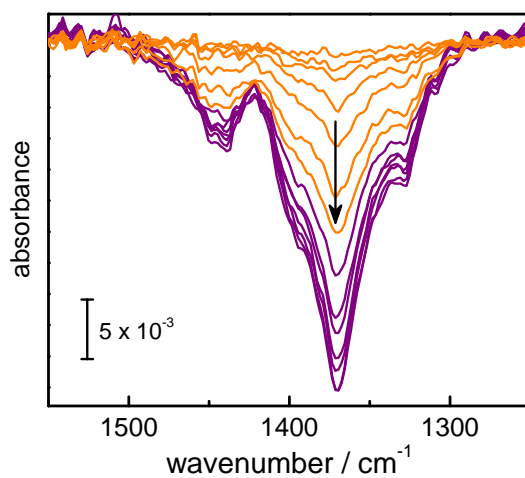
For assignment of the observed vibrational modes and to characterize the corresponding ORR intermediates, selected model structures were computed using DFT. To analyze shifts in the vibrational frequencies of ORR intermediates bound to zinc corrosion products relative to solution species like dissolved oxygen, superoxide and hydrogen peroxide, the focus was on ORR intermediates adsorbed on ZnO. The model structures include two examples of adsorbed oxygen molecules in their triplet ground state, $^3\text{O}_2$, and three examples of adsorbed superoxide anions, $^2\text{O}_2^-$, in the doublet ground state. The superoxide anion is an oxygen molecule after the first reduction step by transfer of one electron. For calculations of solution species and species adsorbed on germanium see the Supplementary Material and Nayak et al., 2013.⁵¹

Fig. 10 visualizes the optimized structures and transition dipole moments of the $\nu(\text{O}-\text{O})$ ($\text{O}-\text{O}$ stretching) modes. Tab. I summarizes important bond lengths and vibrational frequencies.

Fig. 10a represents an oxygen molecule interacting with a undercoordinated Zn site on the non-polar $\text{ZnO}(10\bar{1}0)$ surface: $^3\text{O}_2 @ \text{ZnO}(10\bar{1}0)$. The calculated Zn–O distance of $>3\text{ \AA}$ is very large, indicating a weak interaction. It is much longer than the calculated Zn–O bond lengths, e.g., in bulk ZnO of $1.9\text{-}2.0\text{ \AA}$. Also the interactions with the water molecules



(a)



(b)

FIG. 8: ATR-IR spectra in region 1550-1250 cm⁻¹ in 0.1 M NaClO₄ at pH 10.5 on zinc hydroxide model corrosion products in (a) O₂ and (b) Ar atmosphere. The color changes with time over the course of experiment. Start: (—) at $E = -0.19$ V (initial spectrum; initial polarization in the direction of decreasing potential till -0.79 V). End: (—) at $E = -0.19$ V (last spectrum; after returning from polarization to -0.79 V).

are very weak. There are no hydrogen bonds formed between the oxygen molecule and surrounding water molecules. Therefore, the oxygen molecule is hardly perturbed and its vibrational frequency $\nu(\text{O-O})$ is 1518 cm⁻¹, close to the calculated frequency of an oxygen molecule in vacuum, 1544 cm⁻¹. Nevertheless, the transition dipole moment is substantial, because of symmetry breaking by the environment. We can thus expect peaks in the IR

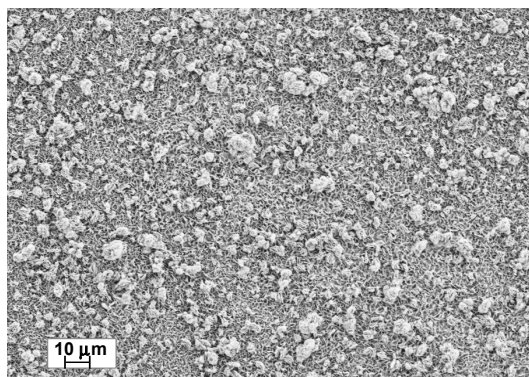


FIG. 9: SEM image of the model corrosion products after ATR-IR electrochemical experiment.

TABLE I: Summary of results obtained by DFT calculations for different adsorbed oxygen species at ZnO surfaces.

#	Species @ Surface ^a	Zn–O (Å) ^b	O–O (Å) ^c	Wavenumber (cm ⁻¹) ^d
(a)	³ O ₂ @ ZnO(10 $\bar{1}$ 0)	3.002	1.220	1518
(b)	³ O ₂ + H ⁺ @ ZnO(10 $\bar{1}$ 0)	2.513	1.246	1322
(c)	² O ₂ ⁻ @ ZnO(10 $\bar{1}$ 0)	2.096	1.337	1157
(d)	² O ₂ ⁻ + H ⁺ @ ZnO(10 $\bar{1}$ 0)	2.119	1.341	1145
(e)	² O ₂ ⁻ @ ZnO(0001)	2.187	1.342	1142

^a See Supplementary Material for a visual representation of the complete structure models.

^b Zn–O bond lengths of the adsorbing oxygen.

^c O–O bond length of the adsorbing species.

^d Vibrational frequency of $\nu(\text{O–O})$ mode.

spectrum even though the $\nu(\text{O–O})$ mode of O₂ is IR inactive in gas phase.

Fig. 10b corresponds to an oxygen molecule co-adsorbed with a proton on the ZnO(10 $\bar{1}$ 0) surface: ³O₂ + H⁺ @ ZnO(10 $\bar{1}$ 0). In this case, the calculated Zn–O distance of ca. 2.5 Å indicates a substantial interaction, although still weaker than a full bond. Furthermore, hydrogen bonds of 2.2-2.6 Å are formed. These interactions result in a substantial shift of

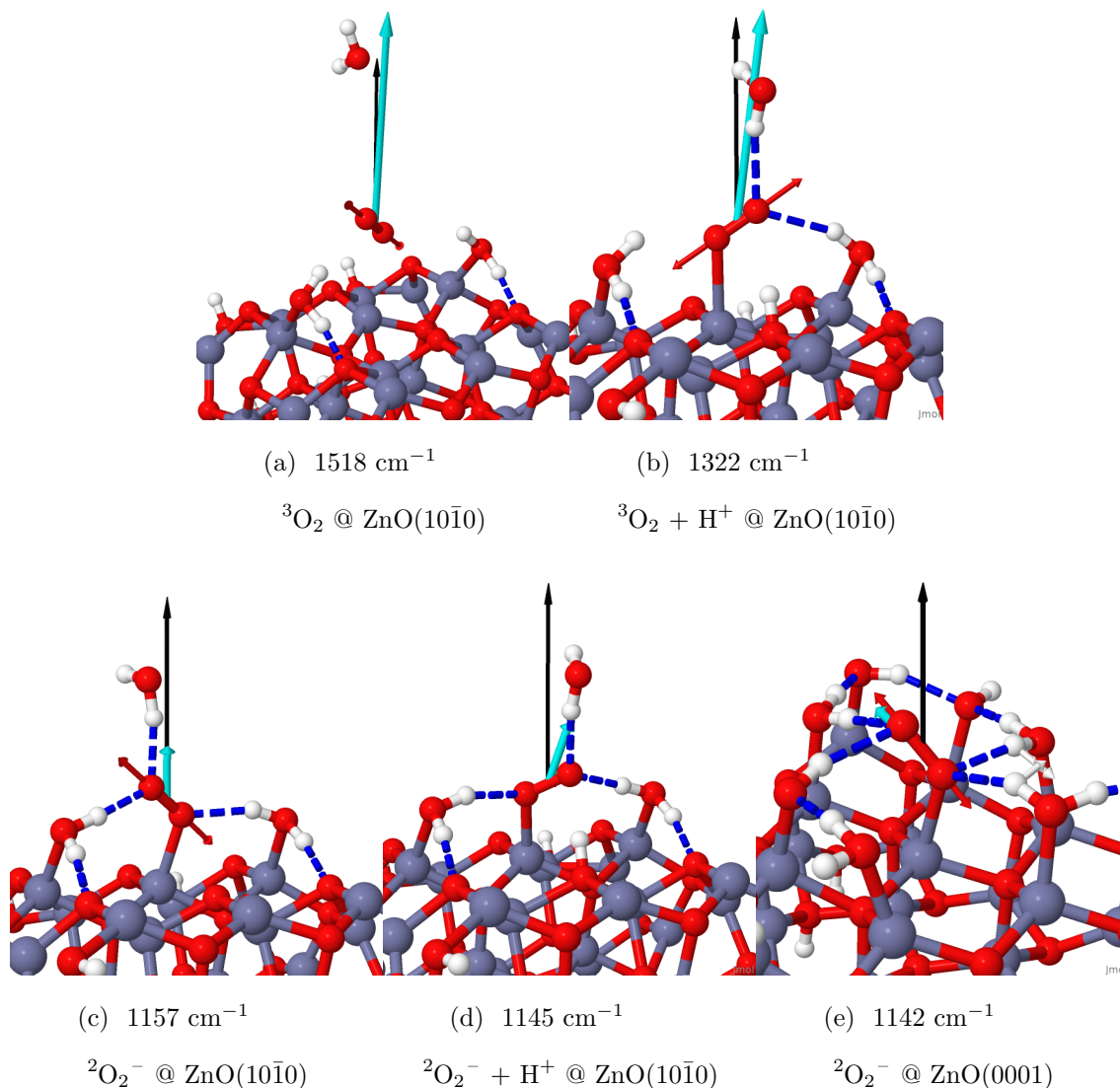


FIG. 10: Structures, atomic displacement during O–O stretching vibration, and transition dipole moment (cyan arrow) for ORR species adsorbed on ZnO: ● - O, ● - Zn, ● - H. The black arrow indicates the surface normal. For images of the full clusters, c.f. Supplementary Material.

the O–O stretching mode [$\nu(\text{O-O}) = 1322 \text{ cm}^{-1}$] by ca. 200 cm^{-1} relative to O_2 in the gas phase.

The structure shown in Fig. 10c consists of a superoxide anion adsorbed on a free Zn surface site: ${}^2\text{O}_2^- @ \text{ZnO}(10\bar{1}0)$. Here, the Zn–O distance of ca. 2.1 \AA is close to the bond length in ZnO indicating a strong adsorption. The hydrogen bonds with neighboring water molecules are short, $1.7\text{-}1.9 \text{ \AA}$, and strong. The O–O bond is 1.3 \AA , compared to ca. 1.2 \AA in

the oxygen molecule. The wavenumber of the $\nu(\text{O}-\text{O})$ is 1157 cm^{-1} in this model structure, shifted by 12 cm^{-1} compared to a superoxide anion in aqueous solution (1145 cm^{-1}).

Fig. 10d shows the structure of a superoxide anion co-adsorbed with a proton on on the $\text{ZnO}(10\bar{1}0)$ facet: ${}^2\text{O}_2^- + \text{H}^+ @ \text{ZnO}(10\bar{1}0)$. This structure may also be interpreted as the precursor for the formation of an adsorbed peroxy radical, ${}^2\text{OOH}$. This calculation was started from an adsorbed peroxy radical, however, during the geometry optimization, the proton transferred to the lone-pair of a close-by surface oxygen, indicating that the surface oxygen is substantially more basic than the superoxide anion. In the optimized structure, the $\text{O}-\text{O}$ bond length is ca. 1.3 \AA . The $\text{Zn}-\text{O}$ distance is ca. 2.1 \AA , close to a bond in ZnO bulk. The distance of the other oxygen to the now surface-bound hydrogen is ca. 2.2 \AA and the $\text{O}-\text{H}$ bond length to the surface oxygen is ca. 1.0 \AA . The hydrogen bonds to neighboring water molecules are $1.7\text{-}1.9\text{ \AA}$. The wavenumber of the $\nu(\text{O}-\text{O})$ is 1145 cm^{-1} , 12 cm^{-1} shifted relative to the structural model (c), and basically identical to the wavenumber of a dissolved superoxide anion.

The model structure in Fig. 10e explores the impact of adsorption on a different type of ZnO surface. The superoxide anion is adsorbed on the zinc-terminated polar (0001) facet: ${}^2\text{O}_2^- @ \text{ZnO}(0001)$. Nevertheless, the $\text{O}-\text{O}$ bond length is ca. 1.3 \AA and the $\text{Zn}-\text{O}$ distance is ca. 2.1 \AA , as in the other adsorbed superoxide anion structures. The hydrogen bonds to neighboring water molecules are $1.8\text{-}2.0\text{ \AA}$, slightly longer than in the other structures. The wavenumber of the $\nu(\text{O}-\text{O})$ is 1142 cm^{-1} , very similar to model (d). Thus, the different ZnO facet has only minor effects on the adsorption structure and the wavenumber of the adsorbed superoxide anion. The effect is comparable to a change in protonation state.

IV. DISCUSSION

A. Spectral interpretation

Only the peak at 1180 cm^{-1} is assigned to an ORR-related species (Tab. II), because it is the only peak that is exclusively observed in O_2 saturated solution and its intensity correlates with the ORR current. All other bands are observed in both Ar as well as O_2 saturated solutions and therefore not related to ORR. In previous works, the vibrational modes observed around $1200\text{-}1230\text{ cm}^{-1}$ were assigned to a Ge-bound superoxide ORR intermediate.^{50,51}

TABLE II: Summary of observed peaks and tentative assignment. sh - shoulder, ν - stretching, δ - deformation, sy - symmetric, as - antisymmetric

Wavenumber cm ⁻¹	Mode assignment	Species
970-980	$\nu_{\text{sy}}(\text{Cl-O})?$	surface-bound perchlorate
1025	$\nu_{\text{as}}(\text{Cl-O})$	surface-bound perchlorate
1050	$\nu_{\text{as}}(\text{Cl-O})$	surface-bound perchlorate
1180	$\nu(\text{O-O})$	superoxide bound to zinc hydroxide / oxide
1325sh	$\nu(\text{N-O})$	nitrate
1380	$\delta(\text{O-H})$	zinc hydroxide
1395sh	$\nu(\text{N-O})$	nitrate
1440	$\delta(\text{NH}_4^+)?$	ammonium?

Based on discussions in our previous works,^{50,51} and the computational results in this work, the vibrational mode at 1180 cm⁻¹ is assigned to a superoxide intermediate bound to the zinc hydroxide model corrosion products. The previous experiments included ORR with isotopically pure 18-oxygen, and showed a shift by ca. 75 cm⁻¹ to lower wavenumber of a mode in this region.⁵⁰ The SERS finding of superoxide at 1150 cm⁻¹ as ORR intermediate on rough Au films,⁷⁶ and the $\nu(\text{O-O})$ wavenumbers calculated for superoxide on ZnO here (Tab. I) also support this interpretation.

The peaks at 1050 cm⁻¹ and 1025 cm⁻¹ were observed in both Ar and O₂ saturated solutions. These two peaks grow simultaneously in absorbance and thus their origin is likely related to the same species. A peak at 1030 cm⁻¹, observed on Ge(100) only in O₂ saturated solution was assigned to a surface-bound perchlorate.⁵¹ Thus, based on previous work, the two bands observed here are assigned to surface-bound perchlorate also.⁵¹ However, perchlorate was found to be bound to the zinc model corrosion products not only during ORR, but also in the Ar purged solution. Its absorbance is not purely related to the potential, i.e. the perchlorate adsorption is not reversible.

The band observed at 1380 cm⁻¹ shows a negative difference absorbance with respect to the first potential in the difference spectra. During ORR on the Ge substrate, a positive

peak observed at 1385 cm^{-1} was assigned to surface-bound peroxide (Ge-OOH),^{50,51} which in this work is not consistent with the observation of this peak in Ar-saturated solution, and with the time-development of the peak. As the prepared model corrosion products contain zinc hydroxide, the absorption at 1380 cm^{-1} may originate from the OH bending mode of zinc hydroxide which changes during the experiment. This spectral feature will also cover possible absorption of the OOH bending modes of peroxide.

The peak at 1440 cm^{-1} may be assigned to a deformation mode of NH_4^+ ,⁷⁷ which is a possible reduction product of the nitrate. The changes during the experiment and the magnitude of the absorbance are not fully consistent with this assignment. Two more shoulders were observed at 1325 cm^{-1} and 1395 cm^{-1} ; these could originate from the stretching vibration of NO_3^- , based on a previous assignment of a mode at 1350 cm^{-1} .⁷⁷ The peak at 1440 cm^{-1} may also have an origin in nitrate with a deviating symmetry.

The increase in absorbance in the region $970\text{-}980\text{ cm}^{-1}$ with more negative potentials, could be caused by the O–O stretching mode of peroxide or the symmetric stretching mode of ClO_4^- .⁵¹ This mode was observed in both Ar and O_2 saturated solution; thus the perchlorate is the more likely origin.

B. Chemical and electrochemical implications

Surface-bound superoxide is observed as the main observable ORR intermediate on zinc hydroxide model corrosion products. The peak position of surface-bound superoxide shifts to lower wavenumber (1180 cm^{-1}) on zinc hydroxide compared to the Ge(100) surface ($1200\text{-}1230\text{ cm}^{-1}$).⁵⁰ The shifting of the band is a clear indication that ORR occurs on the electrodeposited model corrosion product film, and not on the Ge surface, which may be present, e.g., in pinholes in the model corrosion product film. It is also an indirect proof of formation of a closed zinc hydroxide based model corrosion product film on the Ge surface during the electrochemically induced deposition process. The differences in vibrational frequencies between germanium and zinc (hydr)oxide shows the significant effect of the substrate on the bonding situation in the ORR intermediates. The vibrational frequency is still ca. 30 cm^{-1} higher than the calculated value (Tab. I), which is similar to superoxide in aqueous solution; these differences may indicate slight differences in the O–O binding situation in the actual ORR intermediate, possibly due to the much more complex surface situation in the experi-

ments here. Differences may also be due to the approximations in the DFT calculations and the simplifications made in the model structures.

The model corrosion products age with time in a purely chemical process, most likely by condensation in the form $\text{Zn(OH)}_2 \longrightarrow \text{ZnO} + \text{H}_2\text{O}$. The negative difference absorbance of both the OH bending mode and the nitrate modes decrease in a very similar fashion with progressing time. In particular, there is no relation to the flowing current, but rather, changes are slightly larger at the start of the experiment. If the local alkalization related to ORR was responsible for the observed changes, a stronger increase of negative difference absorbance with current would be expected, as larger current implies faster production of OH^- . However, the strong increase in current with negative polarization is not found in a stronger change in these modes at lower potentials. By spectroscopic ellipsometry, our group observed a time evolution consistent with the development of a zinc oxide electronic structure over time for the electrochemically growing oxide layer on zinc.⁷⁸ Also for zinc oxidation under atmospheric conditions, changes in the corrosion product over time were observed.⁷¹ The fact that nitrate is also lost at similar rate as OH indicates that the forming zinc oxide lattice cannot accommodate nitrate ions. The fact that aging processes similar to those for real corrosion products are observed here in the absence of metallic zinc indicates that such aging is a chemical process and does not require supply of Zn^{2+} from oxidizing zinc. The fact that the aging of the corrosion product is realistically mimicking the situation on zinc also shows that the model corrosion products reproduce important aspects of real corrosion products.

We do not see any evidence here for electrochemical nitrate reduction, even though such a reduction cannot be ruled out. However, one would expect a different time-potential-absorbance relationship between OH bending mode and NO stretching mode if the nitrate concentration decreased because of electrochemical reduction; experimentally, however, the related peaks change simultaneously.

The increasing perchlorate adsorption with time is likely also related to the changes in the surface, and the increasing availability of adsorption sites. Increased perchlorate adsorption is evidenced by the irreversible increase in absorbance of perchlorate-related modes. Importantly, the related modes are also observed in Ar-purged solution, which also shows the aging of the model corrosion products, but not the ORR intermediates. Thus, perchlorate adsorption does here not occur as a consequence of ORR and relaxation of active

sites.

The active site for the ORR on ZnO is most likely the undercoordinated, tetrahedral Zn^{2+} site in the zinc oxide surface, which shows a strong interaction in the DFT calculations with the superoxide intermediate after the first electron transfer step. To probe the specific vibration of this bond is challenging in an approach as used here. The respective undercoordinated tetrahedral Zn^{2+} sites are also expected to be present in the complex model corrosion products, in $\text{Zn}(\text{OH})_2$, as well as in ZnO. However, a full study of the complete energetics of all possible intermediates and all possible surface defects was beyond the scope of this work.

The one-electron reduction from ${}^3\text{O}_2$ to ${}^2\text{O}_2^-$ substantially increases the interaction with both, the zinc oxide surface and the surrounding water as reflected by the shorter Zn–O bonds and hydrogen bonds. The enhanced attractive interactions stabilize the reduction product. Therefore, the strong interaction of the superoxide anion with the ZnO surface can be interpreted as a catalytic effect of adsorption on an undercoordinated Zn^{2+} surface site facilitating the first reduction step of the ORR.

V. CONCLUSION

The approach used here, i.e. the deposition of zinc hydroxide model corrosion products on a germanium surface, is successful for studying the ORR on these model corrosion products. An ORR intermediate with an IR absorption at 1180 cm^{-1} has been found on the surfaces of the model corrosion products. The peak was assigned to the O–O stretching mode of a surface-bound superoxide. The absorbance of the detected superoxide is proportional to the cathodic current, indicating a larger surface coverage of the intermediate at higher reaction rates. DFT calculation point to a binding of the superoxide to a undercoordinated tetrahedral Zn^{2+} site on the surface as active center for ORR. The decrease of the Zn–O bond length upon reduction of an adsorbed oxygen molecule to the superoxide anion state indicates an enhanced interaction energy. This state facilitates the reduction reaction and hence corresponds to catalysis of the first reduction step by adsorption on undercoordinated tetrahedral Zn^{2+} surface sites. For the two stable surfaces explored here, the interaction energy did not strongly depend on the surface. Peroxide, a known intermediate in the ORR on zinc corrosion products, couldn't be traced here, because of the overlap of its characteristic

bending mode with the much stronger OH bending mode of the hydroxide in the corrosion products. The DFT calculations give hints on design of successful corrosion inhibitors for zinc: such inhibitors should interact with the active site more strongly than reported here for the adsorbed superoxide.

SUPPLEMENTARY MATERIAL

Images of the complete cluster model structures. Vibrational frequencies of related species in gas phase, solution, and adsorbed to a germanium surface.

ACKNOWLEDGMENTS

S.N. acknowledges the IMPRS Surmat for a scholarship. We thank Petra Ebbinghaus and Natália Vianna Correia for technical support.

AUTHOR DECLARATIONS

Conflict of interest

The authors have no conflicts to disclose.

Author contributions

Simantini Nayak: Data curation (leading); Formal analysis (leading; experimental); Investigation (leading; experimental); Visualization (equal); Writing – original draft (leading)

P. Ulrich Biedermann: Conceptualization (contributing); Data curation (contributing); Formal analysis (contributing; computational); Funding acquisition (contributing); Investigation (contributing; computational); Methodology (contributing); Visualization (equal); Writing – review & editing (contributing)

Andreas Erbe: Conceptualization (leading); Funding acquisition (leading); Methodology (leading); Project administration; Supervision; Writing – review & editing (leading)

Data availability

The data that support the findings of this study are openly available in DataverseNO at <https://doi.org/10.18710/RXKKW0>.

REFERENCES

- ¹K. Kinoshita, *Electrochemical Oxygen Technology*, Electrochemical Society Series, Vol. 1117 (Wiley, New York, 1992).
- ²M.-F. Ng, D. J. Blackwood, H. Jin, and T. L. Tan, “Tuning oxygen reduction activity on chromia surface via alloying: a DFT study,” *Chem. - Asian J.* **15**, 4087–4092 (2020).
- ³R. Krieg, M. Rohwerder, S. Evers, B. Schuhmacher, and J. Schauer-Pass, “Cathodic self-healing at cut-edges: The effect of Zn²⁺ and Mg²⁺ ions,” *Corros. Sci.* **65**, 119–127 (2012).
- ⁴X. G. Zhang, *Corrosion and electrochemistry of zinc* (Plenum Press, New York, 1996).
- ⁵S. Thomas, I. S. Cole, Y. Gonzalez-Garcia, M. Chen, M. Musameh, J. M. C. Mol, H. Terryn, and N. Birbilis, “Oxygen consumption upon electrochemically polarised zinc,” *J. Appl. Electrochem.* **44**, 747–757 (2014).
- ⁶J. Stoullil, T. Prosek, A. Nazarov, J. Oswald, P. Kriz, and D. Thierry, “Electrochemical properties of corrosion products formed on Zn-Mg, Zn-Al and Zn-Al-Mg coatings in model atmospheric conditions,” *Mater. Corros.* **66**, 777–782 (2015).
- ⁷M. Salgueiro Azevedo, C. Allély, K. Ogle, and P. Volovitch, “Corrosion mechanisms of Zn(Mg,Al) coated steel: 2. the effect of Mg and Al alloying on the formation and properties of corrosion products in different electrolytes,” *Corros. Sci.* **90**, 482–490 (2015).
- ⁸D. Persson, D. Thierry, N. LeBozec, and T. Prosek, “In situ infrared reflection spectroscopy studies of the initial atmospheric corrosion of Zn–Al–Mg coated steel,” *Corros. Sci.* **72**, 54–63 (2013).
- ⁹A. Nazarov, E. Diler, D. Persson, and D. Thierry, “Electrochemical and corrosion properties of ZnO/Zn electrode in atmospheric environments,” *J. Electroanal. Chem.* **737**, 129–140 (2015).
- ¹⁰A. Nazarov, D. Thierry, and T. Prosek, “Formation of Galvanic Cells and Localized Corrosion of Zinc and Zinc Alloys Under Atmospheric Conditions,” *Corrosion* **73**, 77–86

- (2016).
- ¹¹Y. Chen, P. Schneider, B.-J. Liu, S. Borodin, B. Ren, and A. Erbe, “Electronic structure and morphology of dark oxides on zinc generated by electrochemical treatment,” *Phys. Chem. Chem. Phys.* **15**, 9812–9822 (2013).
- ¹²D. Iqbal, A. Sarfraz, and A. Erbe, “Gradient in defect density of ZnO nanorods grown by cathodic delamination, a corrosion process, leads to end-specific luminescence,” *Nanoscale Horiz.* **3**, 58–65 (2018).
- ¹³R. Tena-Zaera, J. Elias, C. Lévy-Clément, C. Bekeny, T. Voss, I. Mora-Seró, and J. Bisquert, “Influence of the potassium chloride concentration on the physical properties of electrodeposited ZnO nanowire arrays,” *J. Phys. Chem. C* **112**, 16318–16323 (2008).
- ¹⁴A. Altin, M. Krzywiecki, A. Sarfraz, C. Toparli, C. Laska, P. Kerger, A. Zeradjanin, K. J. J. Mayrhofer, M. Rohwerder, and A. Erbe, “Cyclodextrin inhibits zinc corrosion by destabilizing point defect formation in the oxide layer,” *Beilstein J. Nanotechnol.* **9**, 936–944 (2018).
- ¹⁵R. Grothe, J. Striewe, D. Meinderink, T. Tröster, and G. Grundmeier, “Enhanced corrosion resistance of adhesive/galvanised steel interfaces by nanocrystalline ZnO thin film deposition and molecular adhesion promoting films,” *J. Adhes.* , 1–21 (2021).
- ¹⁶P. Kalinauskas, I. Valsiūnas, M. Samulevičien, and E. Juzeliūnas, “Zinc photo-corrosion in neutral solutions,” *Corros. Sci.* **43**, 2083–2092 (2001).
- ¹⁷H. Wilson and A. Erbe, “Convection induced by illumination-based metal surface heating increases corrosion potential, corrosion rates,” *Electrochem. Commun.* **106**, 106513 (2019).
- ¹⁸F. Su, P. Zhang, D. Wei, X. Chen, F. Ding, and B. Wang, “Corrosion behavior of hot-dip Al–Zn coating doped with Si, RE, and Mg during exposure to sodium chloride containing environments,” *Mater. Corros.* **69**, 714–724 (2018).
- ¹⁹K. Bae, J. La, K. Kim, and S. Lee, “Effects of immersion time in 3.5 wt.% NaCl solution on the corrosion characteristics of the ZnMg coated steel,” *Sci. Adv. Mater.* **9**, 881–887 (2017).
- ²⁰J. Han and K. Ogle, “Dealloying of MgZn₂ intermetallic in slightly alkaline chloride electrolyte and its significance in corrosion resistance,” *J. Electrochem. Soc.* **164**, C952–C961 (2017).
- ²¹T. Prosek, D. Persson, J. Stoullil, and D. Thierry, “Composition of corrosion products formed on Zn–Mg, Zn–Al and Zn–Al–Mg coatings in model atmospheric conditions,” *Cor-*

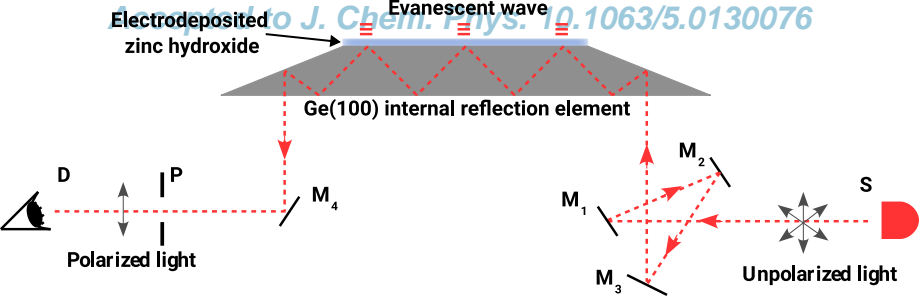
- ros. Sci. **86**, 231–238 (2014).
- ²²M. Prestat, J. Soares Costa, B. Lescop, S. Rioual, L. Holzer, and D. Thierry, “Cathodic corrosion of zinc under potentiostatic conditions in NaCl solutions,” *ChemElectroChem* **5**, 1203–1211 (2018).
- ²³M. Li, N. Qin, Z. Ji, Q. Gan, Z. Wang, Y. Li, L. Cao, H. Yuan, D. He, Z. Chen, G. Luo, K. Zhang, and Z. Lu, “Single copper sites dispersed on defective TiO_{2-x} as a synergistic oxygen reduction reaction catalyst,” *J. Chem. Phys.* **154**, 034705 (2021).
- ²⁴W. Fürbeth and M. Stratmann, “Scanning Kelvinprobe investigations on the delamination of polymeric coatings from metallic surfaces,” *Prog. Org. Coat.* **39**, 23–29 (2000).
- ²⁵W. Fürbeth and M. Stratmann, “The delamination of polymeric coatings from electrogalvanised steel – a mechanistic approach.: Part 1: delamination from a defect with intact zinc layer,” *Corros. Sci.* **43**, 207–227 (2001).
- ²⁶C. D. Fernández-Solis, A. Vimalanandan, A. Altin, J. S. Mondragón-Ochoa, K. Kreth, P. Keil, and A. Erbe, “Fundamentals of Electrochemistry, Corrosion and Corrosion Protection,” in *Soft Matter at Aqueous Interfaces*, Lecture Notes in Physics, Vol. 917, edited by P. R. Lang and Y. Liu (Springer, Cham, Switzerland, 2016) pp. 29–70.
- ²⁷D. Iqbal, A. Sarfraz, M. Stratmann, and A. Erbe, “Solvent-starved conditions in confinement cause chemical oscillations excited by passage of a cathodic delamination front,” *Chem. Commun.* **51**, 16041–16044 (2015).
- ²⁸R. Posner, G. Giza, R. Vlasak, and G. Grundmeier, “In situ electrochemical scanning Kelvin probe blister-test studies of the de-adhesion kinetics at polymer/zinc oxide/zinc interfaces,” *Electrochim. Acta* **54**, 4837–4843 (2009).
- ²⁹R. Posner, K. Wapner, M. Stratmann, and G. Grundmeier, “Transport processes of hydrated ions at polymer/oxide/metal interfaces: Part 1. transport at interfaces of polymer coated oxide covered iron and zinc substrates,” *Electrochim. Acta* **54**, 891–899 (2009).
- ³⁰G. Williams, H. N. McMurray, and M. J. Loveridge, “Inhibition of corrosion-driven organic coating disbondment on galvanised steel by smart release group II and zn(II)-exchanged bentonite pigments,” *Electrochim. Acta* **55**, 1740–1748 (2010).
- ³¹K. Ogle, S. Morel, and N. Meddahi, “An electrochemical study of the delamination of polymer coatings on galvanized steel,” *Corros. Sci.* **47**, 2034–2052 (2005).
- ³²G. Klimow, N. Fink, and G. Grundmeier, “Electrochemical studies of the inhibition of the cathodic delamination of organically coated galvanised steel by thin conversion films,”

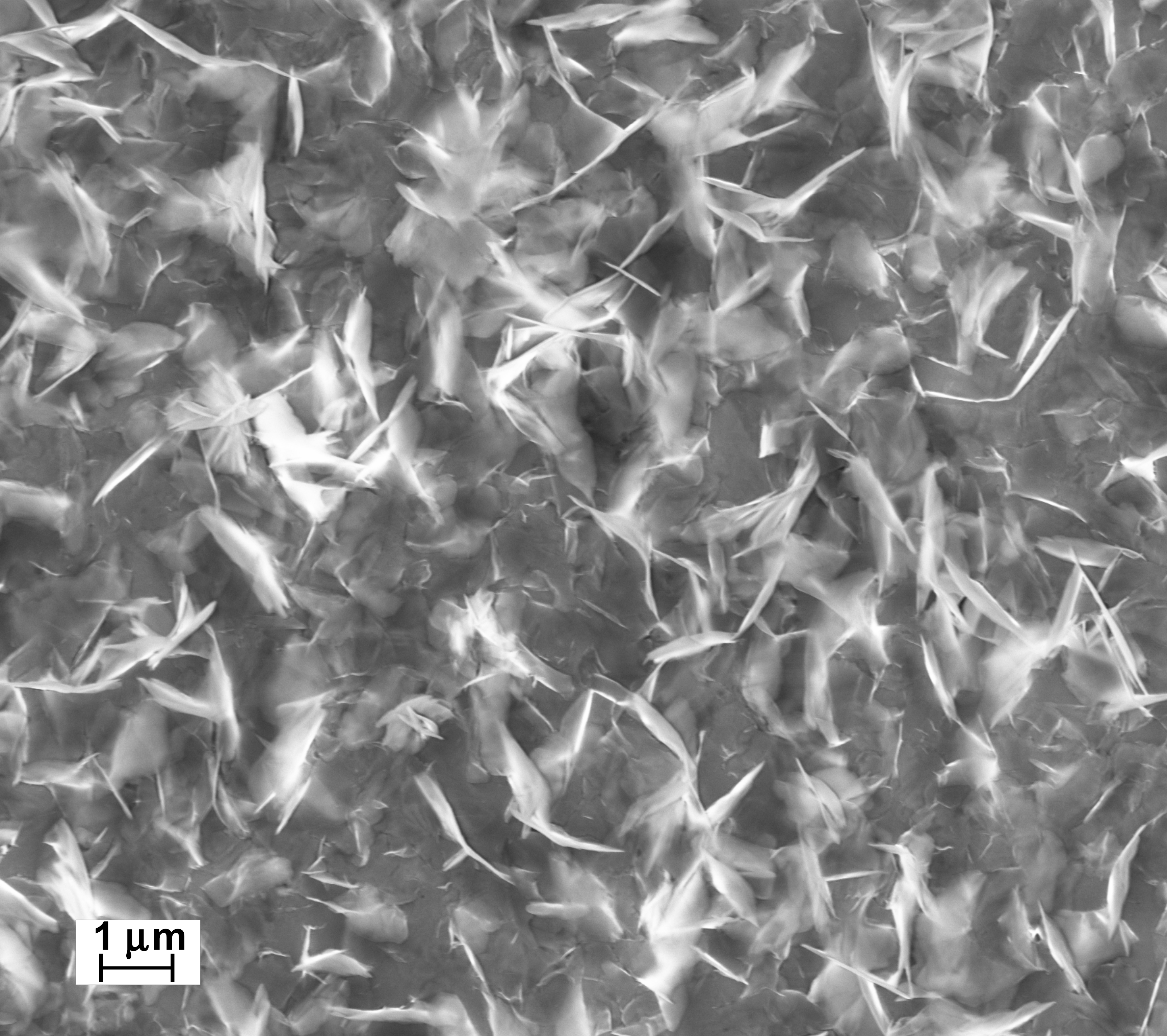
- Electrochim. Acta **53**, 1290–1299 (2007).
- ³³D. Iqbal, J. Rechmann, A. Sarfraz, A. Altin, G. Genchev, and A. Erbe, “Synthesis of ultrathin poly(methyl methacrylate) model coatings bound via organosilanes to zinc and investigation of their delamination kinetics,” *ACS Appl. Mater. Interfaces* **6**, 18112–18121 (2014).
- ³⁴D. Iqbal, R. S. Moirangthem, A. Bashir, and A. Erbe, “Study of polymer coating delamination kinetics on zinc modified with zinc oxide of different morphologies,” *Mater. Corros.* **65**, 370–375 (2014).
- ³⁵D. Iqbal, J. Rechmann, A. Bashir, A. Sarfraz, A. Altin, and A. Erbe, “Cathodic delamination kinetics of thin polystyrene model coatings bound to zinc via organosilanes,” *Mater. Corros.* **70**, 481–491 (2019).
- ³⁶G. Williams, H. N. McMurray, and A. Bennett, “Inhibition of corrosion-driven organic coating delamination from a zinc surface using polyaniline pigments,” *Mater. Corros.* **65**, 401–409 (2014).
- ³⁷Y. Luo, A. Vimalanandan, X. Wang, and M. Rohwerder, “Study of the buried interface between zinc and emeraldine base coating,” *Electrochim. Acta* **161**, 10–16 (2015).
- ³⁸H. Wroblowa, “Intermediate products of atmospheric oxygen reduction and the integrity of metal—organic coating interface,” *J. Electroanal. Chem.* **339**, 31–40 (1992).
- ³⁹A. Altin, M. Rohwerder, and A. Erbe, “Cyclodextrins as carriers for organic corrosion inhibitors in organic coatings,” *J. Electrochem. Soc.* **164**, C128–C134 (2017).
- ⁴⁰A. Altin, A. Vimalanandan, A. Sarfraz, M. Rohwerder, and A. Erbe, “Pretreatment with a β -cyclodextrin-corrosion inhibitor complex stops an initiated corrosion process on zinc,” *Langmuir* **35**, 70–77 (2019).
- ⁴¹D. Iqbal, A. Kostka, A. Bashir, A. Sarfraz, Y. Chen, A. D. Wieck, and A. Erbe, “Sequential growth of zinc oxide nanorod arrays at room temperature via a corrosion process: Application in visible light photocatalysis,” *ACS Appl. Mater. Interfaces* **6**, 18728–18734 (2014).
- ⁴²G. Yi, X. Li, Y. Yuan, and Y. Zhang, “Redox active Zn/ZnO duo generating superoxide ($\cdot\text{O}_2^-$) and H_2O_2 under all conditions for environmental sanitation,” *Environ. Sci.: Nano* **6**, 68–74 (2019).
- ⁴³A. S. Saratovskii, K. Y. Senchik, A. V. Karavaeva, S. K. Evstropiev, and N. V. Nikonorov, “Photo-oxygenation of water media using photoactive plasmonic nanocomposites,” *J.*

- Chem. Phys. **156**, 201103 (2022).
- ⁴⁴L. Long, Q. Wu, Q. Chao, Y. Dong, L. Wu, Q. Zhang, Y. Zhou, and D. Wang, “Surface-state-mediated interfacial charge dynamics between carbon dots and ZnO toward highly promoting photocatalytic activity,” *J. Chem. Phys.* **153**, 044708 (2020).
- ⁴⁵M. Prestat, F. Vucko, B. Lescop, S. Rioual, F. Peltier, and D. Thierry, “Oxygen reduction at electrodeposited ZnO layers in alkaline solution,” *Electrochim. Acta* **218**, 228–236 (2016).
- ⁴⁶Z. Pilbáth and L. Sziráki, “The electrochemical reduction of oxygen on zinc corrosion films in alkaline solutions,” *Electrochim. Acta* **53**, 3218–3230 (2008).
- ⁴⁷A. P. Yadav, A. Nishikata, and T. Tsuru, “Oxygen reduction mechanism on corroded zinc,” *J. Electroanal. Chem.* **585**, 142–149 (2005).
- ⁴⁸H. Dafydd, D. A. Worsley, and H. N. McMurray, “The kinetics and mechanism of cathodic oxygen reduction on zinc and zinc–aluminium alloy galvanized coatings,” *Corros. Sci.* **47**, 3006–3018 (2005).
- ⁴⁹H. H. Hassan, “Perchlorate and oxygen reduction during Zn corrosion in a neutral medium,” *Electrochim. Acta* **51**, 5966–5972 (2006).
- ⁵⁰S. Nayak, P. U. Biedermann, M. Stratmann, and A. Erbe, “In situ infrared spectroscopic investigation of intermediates in the electrochemical oxygen reduction on n-Ge(100) in alkaline perchlorate and chloride electrolyte,” *Electrochim. Acta* **106**, 472–482 (2013).
- ⁵¹S. Nayak, P. U. Biedermann, M. Stratmann, and A. Erbe, “A mechanistic study of the electrochemical oxygen reduction on the model semiconductor n-Ge(100) by ATR-IR and DFT,” *Phys. Chem. Chem. Phys.* **15**, 5771–5781 (2013).
- ⁵²S. Nayak, I. J. McPherson, and K. A. Vincent, “Adsorbed intermediates in oxygen reduction on platinum nanoparticles observed by in situ IR spectroscopy,” *Angew. Chem. Int. Ed.* **57**, 12855–12858 (2018).
- ⁵³S. Pletincx, J. M. Mol, H. Terryn, A. Hubin, and T. Hauffman, “An in situ spectro-electrochemical monitoring of aqueous effects on polymer/metal oxide interfaces,” *J. Electroanal. Chem.* **848**, 113311 (2019).
- ⁵⁴L. Fockaert, S. Pletincx, D. Ganzinga-Jurg, B. Boelen, T. Hauffman, H. Terryn, and J. Mol, “Chemisorption of polyester coatings on zirconium-based conversion coated multi-metal substrates and their stability in aqueous environment,” *Appl. Surf. Sci.* **508**, 144771 (2020).

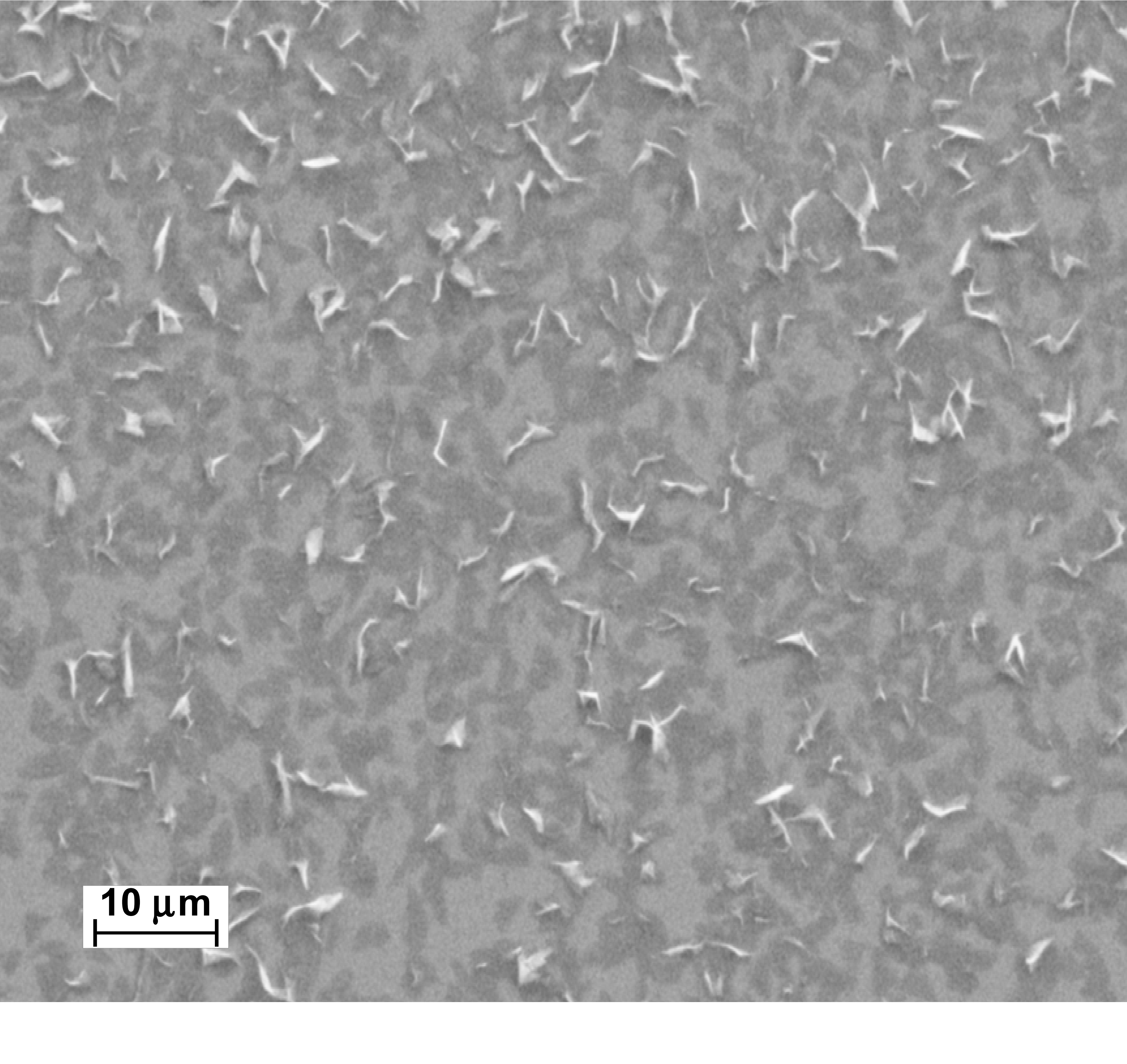
- ⁵⁵S. Kenmoe and P. U. Biedermann, “Water adsorbate phases on ZnO and impact of vapor pressure on the equilibrium shape of nanoparticles,” *J. Chem. Phys.* **148**, 054701 (2018).
- ⁵⁶F. Haque, S. Chenot, F. Viñes, F. Illas, S. Stankic, and J. Jupille, “ZnO powders as multi-facet single crystals,” *Phys. Chem. Chem. Phys.* **19**, 10622–10628 (2017).
- ⁵⁷C. Wöll, “The chemistry and physics of zinc oxide surfaces,” *Prog. Surf. Sci.* **82**, 55–120 (2007).
- ⁵⁸T. Yoshida, D. Komatsu, N. Shimokawa, and H. Minoura, *Thin Solid Films* **451-452**, 166–169 (2004).
- ⁵⁹F. Niu, M. Rabe, S. Nayak, and A. Erbe, “Vibrational spectroscopic study of ph dependent solvation at a ge(100)-water interface during an electrode potential triggered surface termination transition,” *J. Chem. Phys.* **148**, 222824 (2018).
- ⁶⁰S. Nayak, P. U. Biedermann, and A. Erbe, “Replication data for: “Superoxide intermediate in the oxygen reduction on a zinc hydroxide model corrosion product”,,” NTNU Open Research Data, <https://doi.org/10.18710/RXKKWO> (2022).
- ⁶¹I. Horcas, R. Fernández, J. M. Gómez-Rodríguez, J. Colchero, J. Gómez-Herrero, and A. M. Baro, “WSXM: A software for scanning probe microscopy and a tool for nanotechnology,” *Rev. Sci. Instrum.* **78**, 013705 (2007).
- ⁶²F. Viñes, A. Iglesias-Juez, F. Illas, and M. Fernández-García, “Hydroxyl identification on ZnO by infrared spectroscopies: Theory and experiments,” *J. Phys. Chem. C* **118**, 1492–1505 (2014).
- ⁶³S. Kenmoe and P. U. Biedermann, “Water aggregation and dissociation on the ZnO(10 $\bar{1}$ 0) surface,” *Phys. Chem. Chem. Phys.* **19**, 1466–1486 (2017).
- ⁶⁴A. D. Becke, “Density-functional exchange-energy approximation with correct asymptotic behavior,” *Phys. Rev. A* **38**, 3098–3100 (1988).
- ⁶⁵J. P. Perdew, “Density-functional approximation for the correlation energy of the inhomogeneous electron gas,” *Phys. Rev. B* **33**, 8822–8824 (1986).
- ⁶⁶F. Weigend and R. Ahlrichs, “Balanced basis sets of split valence, triple zeta valence and quadruple zeta valence quality for H to Rn: Design and assessment of accuracy,” *Phys. Chem. Chem. Phys.* **7**, 3297–3305 (2005).
- ⁶⁷A. Klamt and G. Schuurmann, “COSMO: a new approach to dielectric screening in solvents with explicit expressions for the screening energy and its gradient,” *J. Chem. Soc., Perkin Trans. 2*, 799–805 (1993).

- ⁶⁸A. Klamt, “Calculation of UV/Vis spectra in solution,” J. Phys. Chem. **100**, 3349–3353 (1996).
- ⁶⁹“TURBOMOLE V6.2 2010, a development of University of Karlsruhe and Forschungszentrum Karlsruhe GmbH, 1989-2007, TURBOMOLE GmbH, since 2007; available from <http://www.turbomole.com>.” (2014).
- ⁷⁰W. Stählin and H. R. Oswald, “The crystal structure of zinc hydroxide nitrate, $\text{Zn}_5(\text{OH})_8(\text{NO}_3)_2 \cdot 2\text{H}_2\text{O}$,” Acta Crystallogr. Sect. B **26**, 860–863 (1970).
- ⁷¹Y. Chen, P. Schneider, and A. Erbe, “Investigation of native oxide growth on zinc in different atmospheres by spectroscopic ellipsometry,” Phys. Status Solidi A **209**, 846–853 (2012).
- ⁷²S. Lany and A. Zunger, “Dopability, intrinsic conductivity, and nonstoichiometry of transparent conducting oxides,” Phys. Rev. Lett. **98**, 045501 (2007).
- ⁷³J. Zuo and A. Erbe, “Optical and electronic properties of native zinc oxide films on polycrystalline Zn,” Phys. Chem. Chem. Phys. **12**, 11467–11476 (2010).
- ⁷⁴S. W. Gaarenstroom and N. Winograd, “Initial and final state effects in the ESCA spectra of cadmium and silver oxides,” J. Chem. Phys. **67**, 3500–3506 (1977).
- ⁷⁵J. F. Moulder, W. Stickle, P. E. Sobol, and K. D. Bomben, *Handbook of X-ray Photoelectron Spectroscopy* (Physical Electronics, 1995).
- ⁷⁶J. Kim and A. A. Gewirth, J. Phys. Chem. B **110**, 2565–2571 (2006).
- ⁷⁷G. J. Boer, I. N. Sokolika, and S. Martin, J. Quant. Spectrosc. Rad. Transfer **108**, 17 (2007).
- ⁷⁸Y. Chen and A. Erbe, “In situ spectroscopic ellipsometry during electrochemical treatment of zinc in alkaline carbonate electrolyte,” Surf. Sci. **607**, 39–46 (2013).

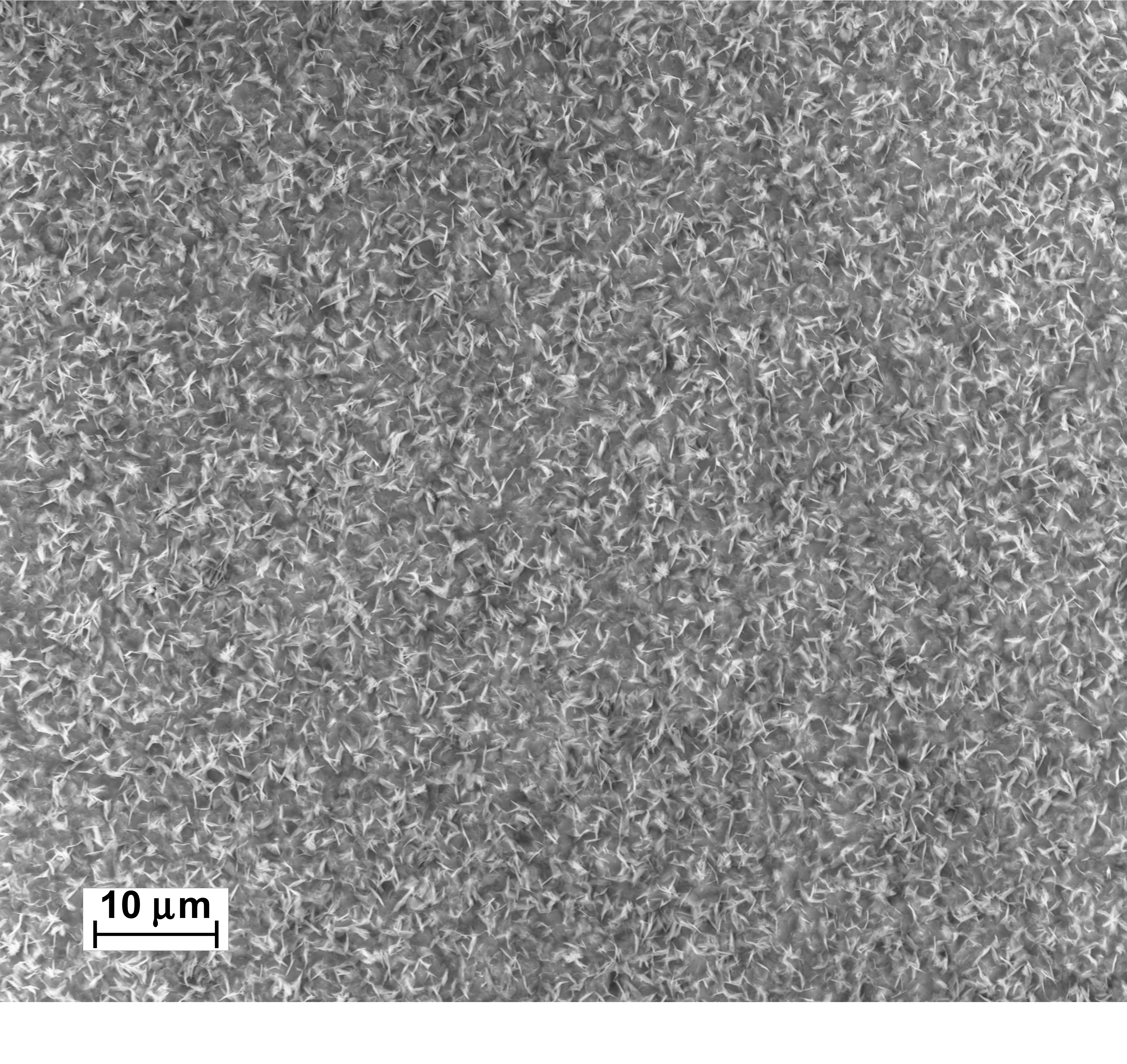




1 μm

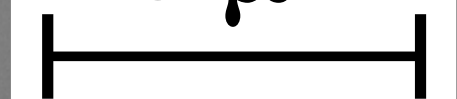


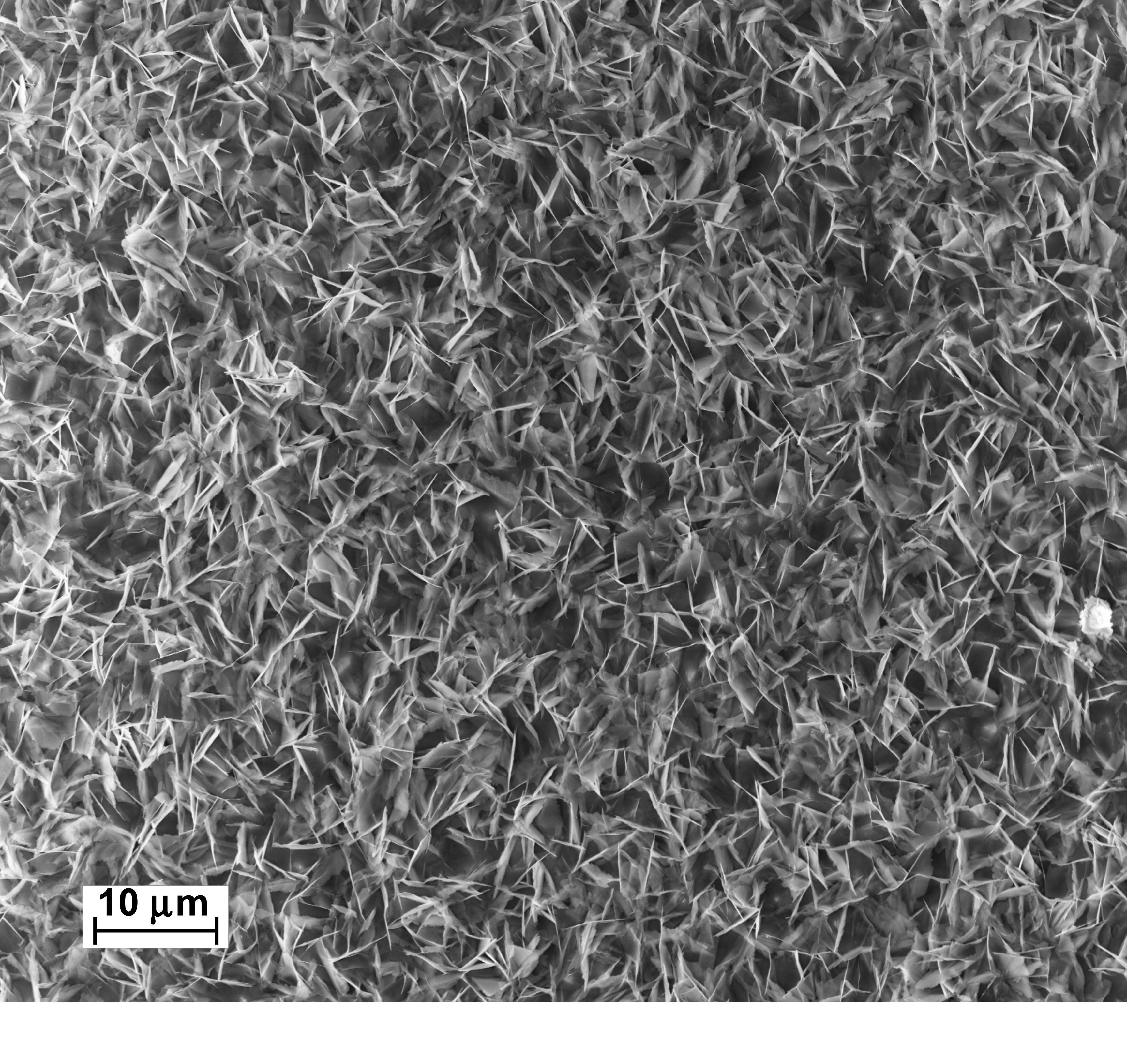
10 μm



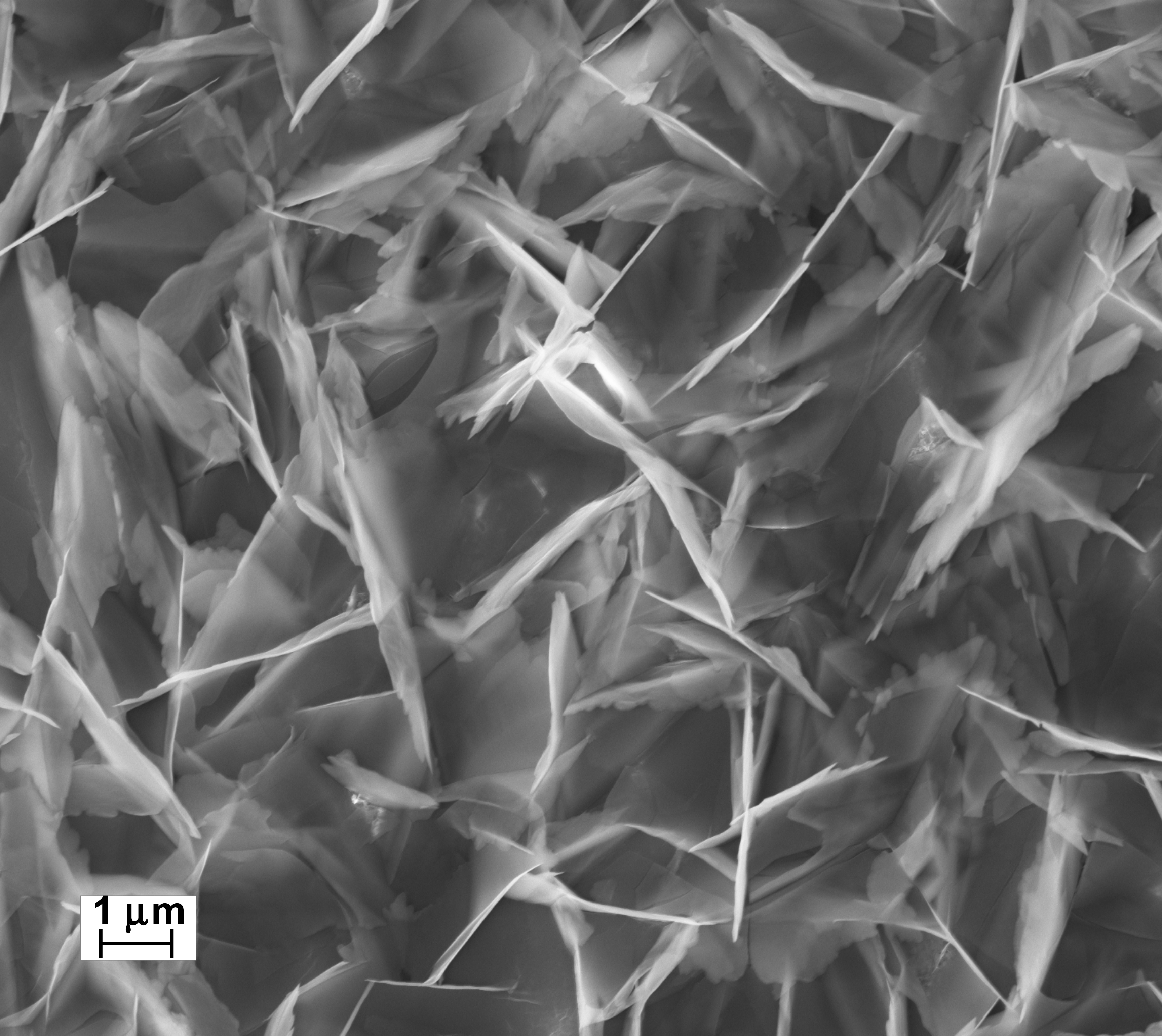
10 μm

10 μm





10 μm



1 μm

Intensity / a.u.

Accepted to J.

Zn

Ge

O

0

2

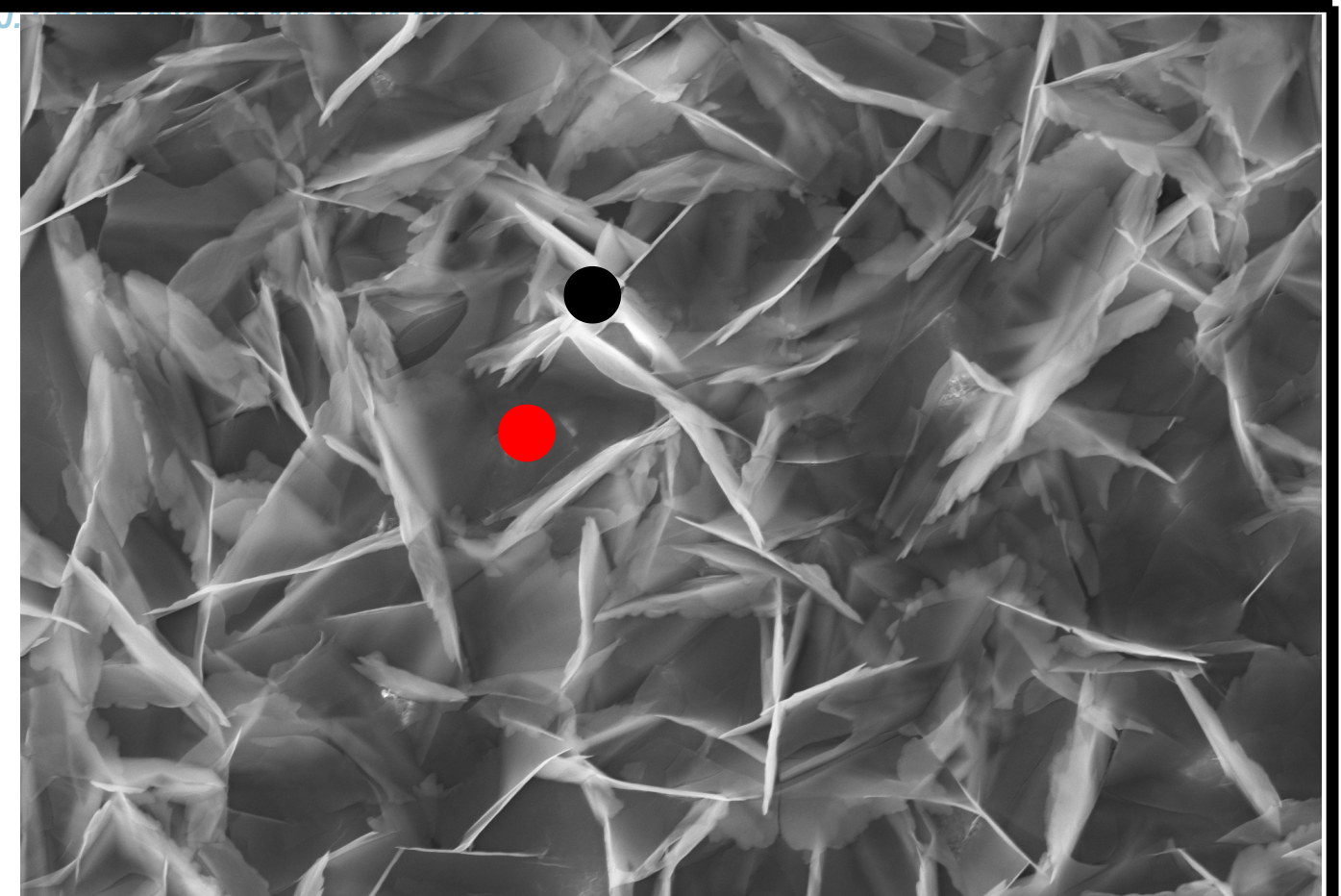
4

6

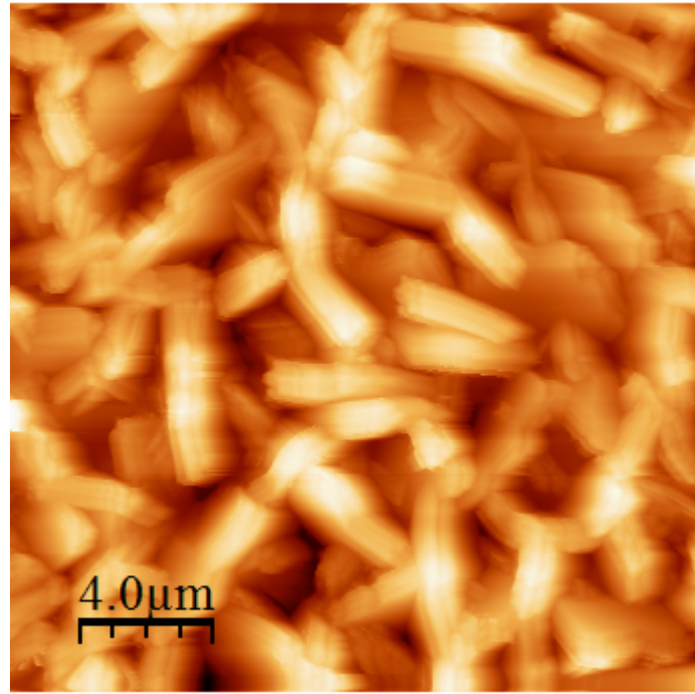
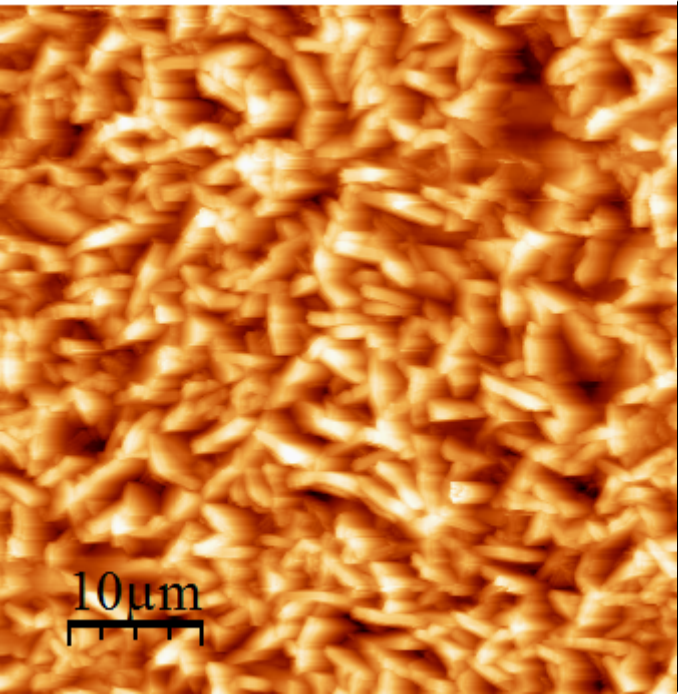
8

10

Energy / keV

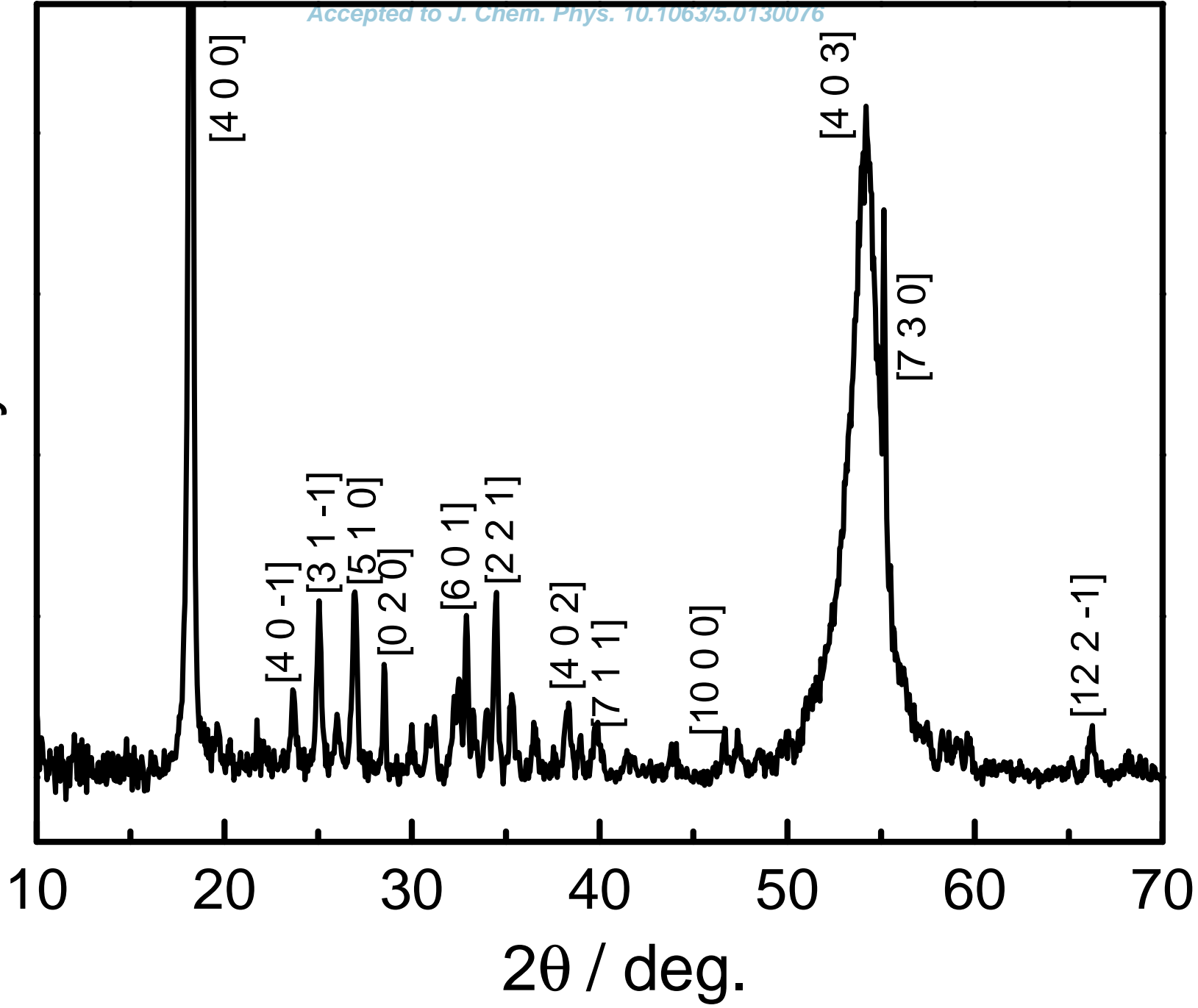


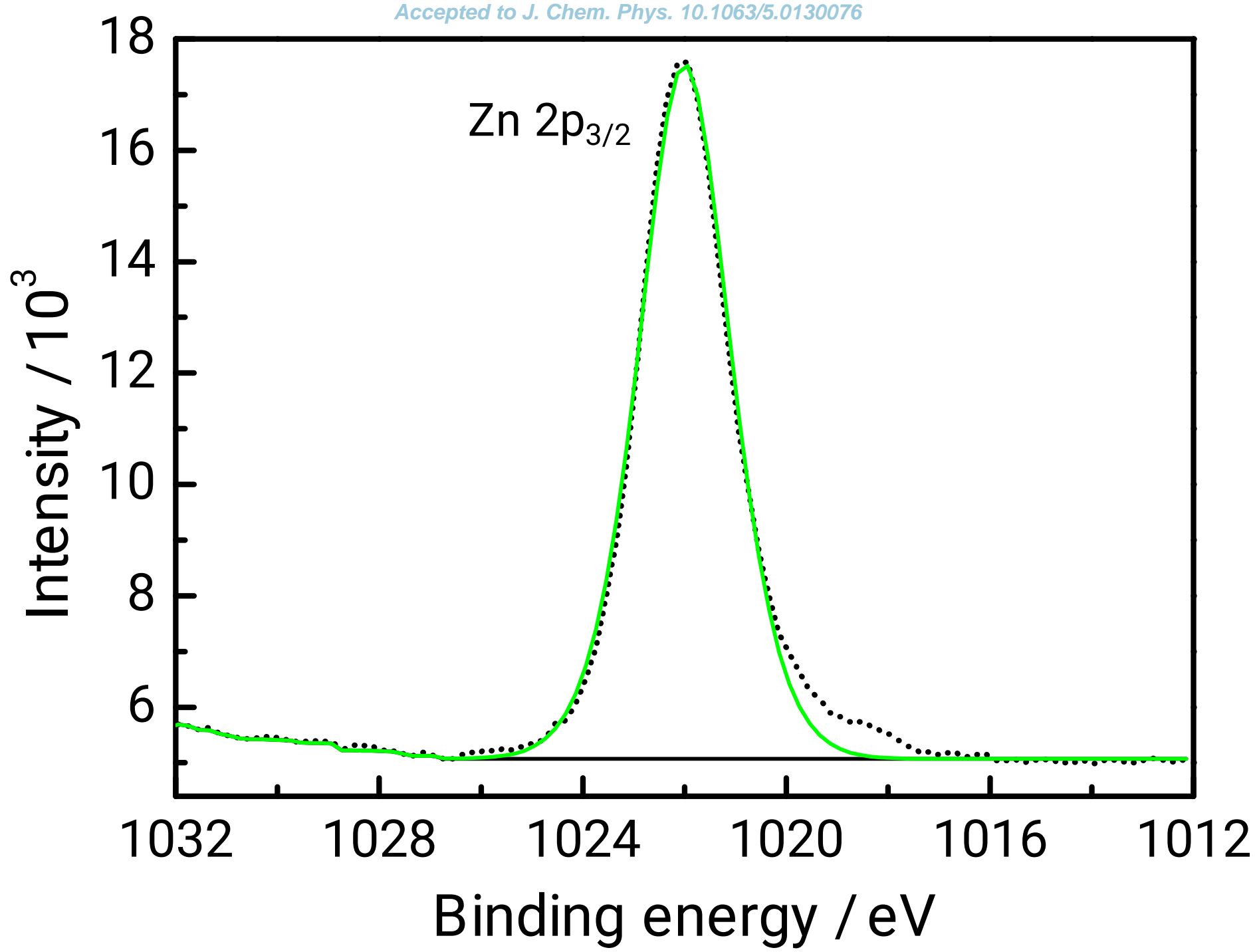
2.88 μm

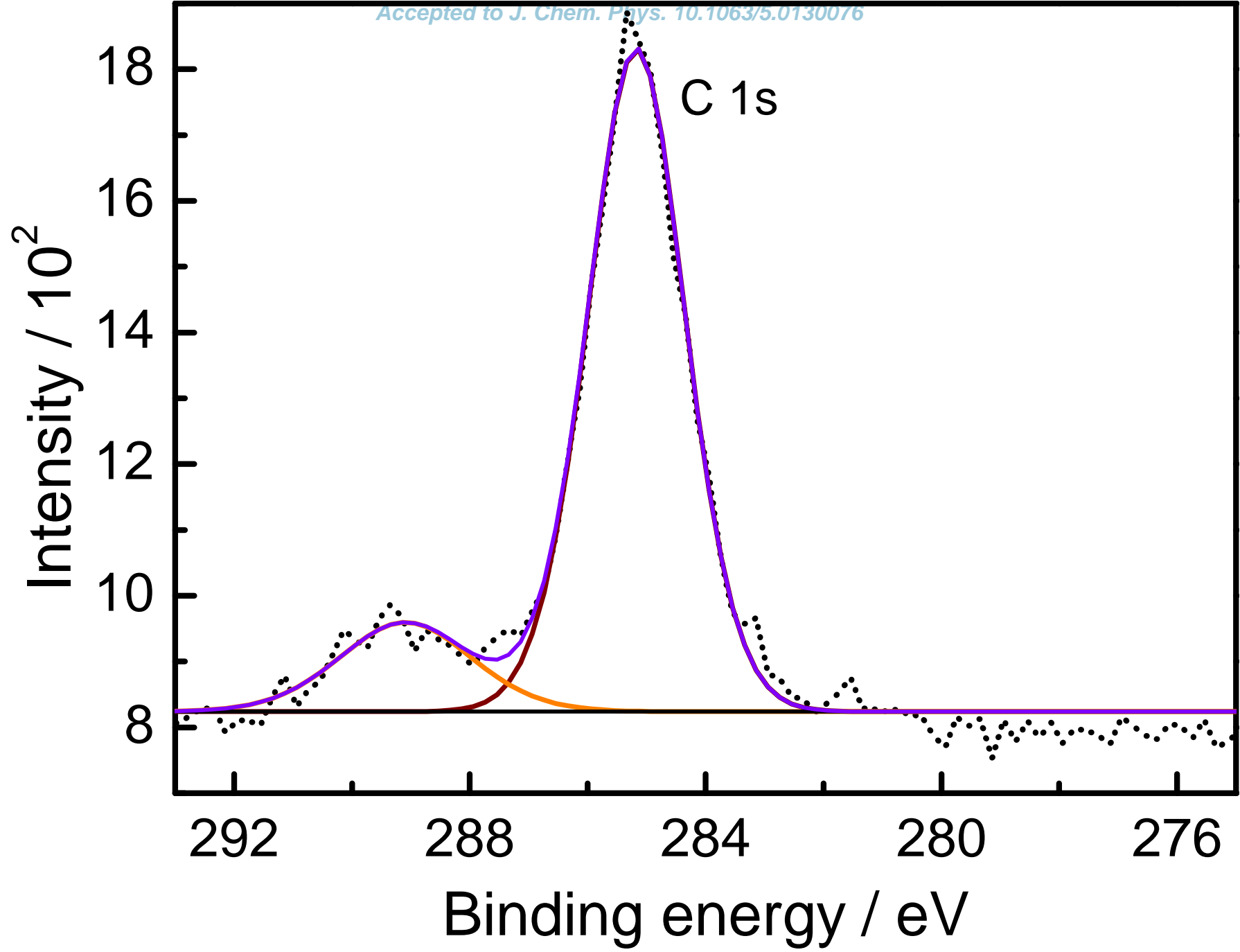


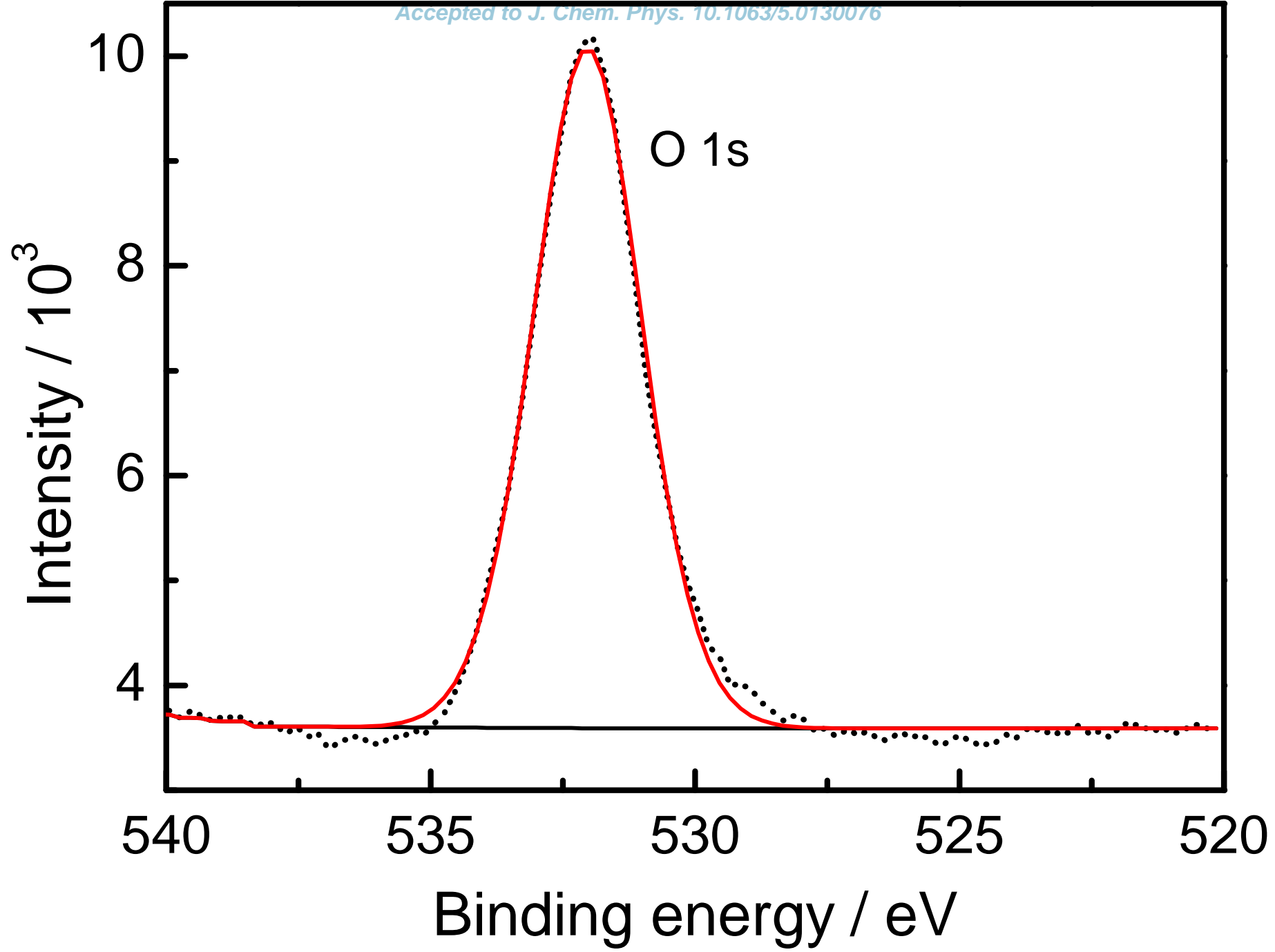
2.9 μm

Intensity / a.u.

 2θ / deg.







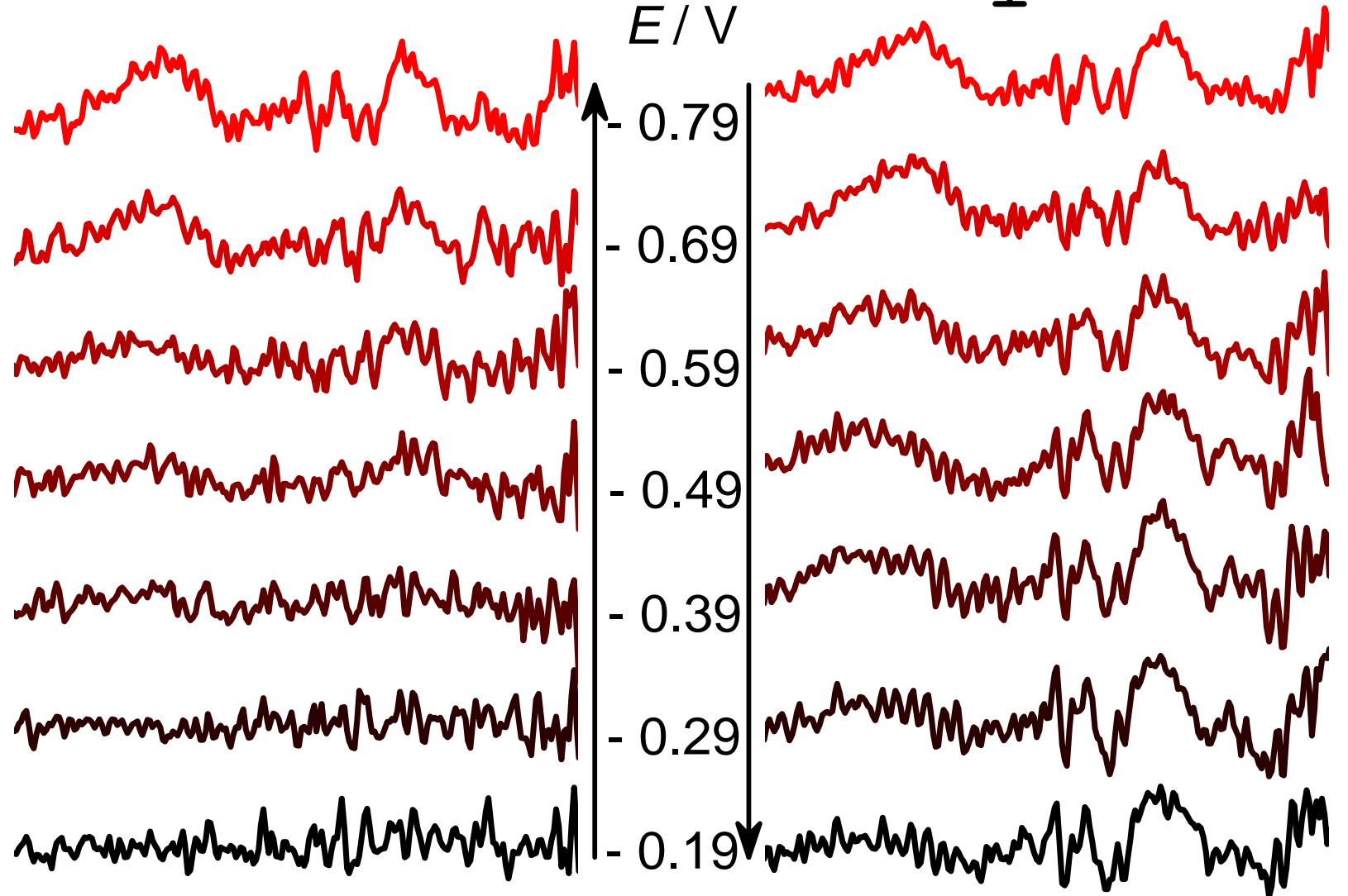
O_2 2.5×10^{-3} E / V

absorbance

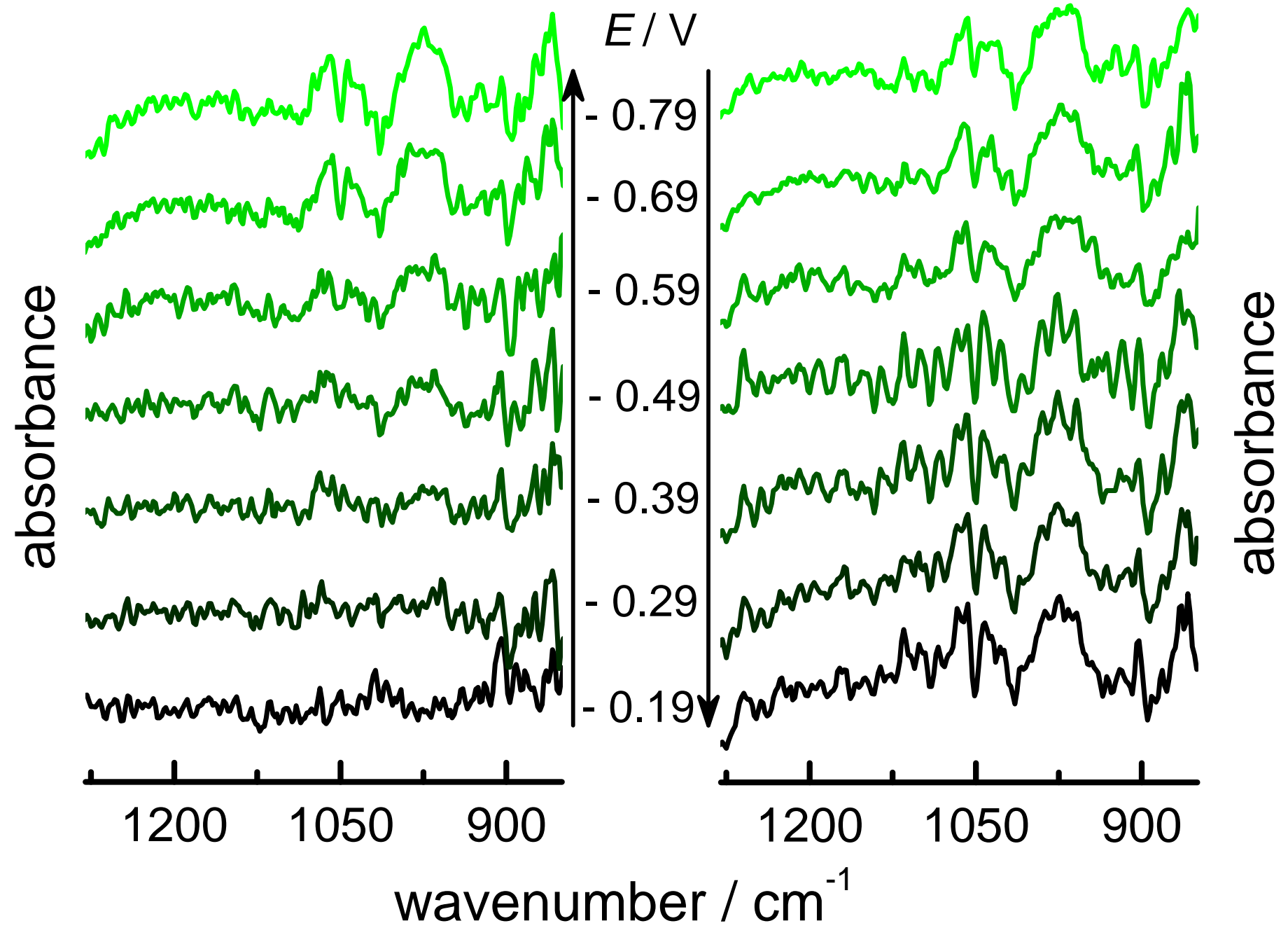
absorbance

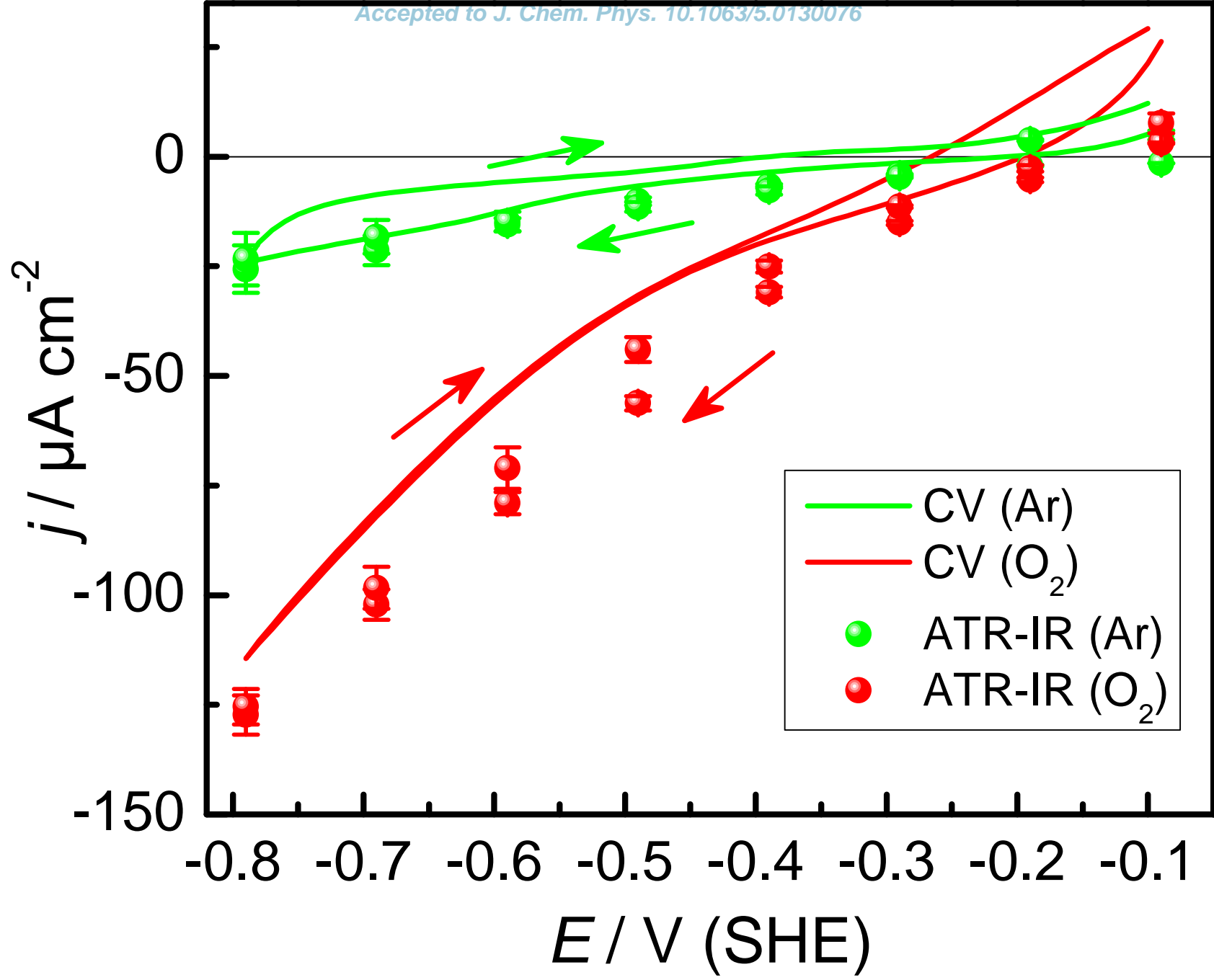
-0.79
-0.69
-0.59
-0.49
-0.39
-0.29
-0.19

1200 1050 900 1200 1050 900

wavenumber / cm^{-1} 

Ar

 2.5×10^{-3} 



absorbance

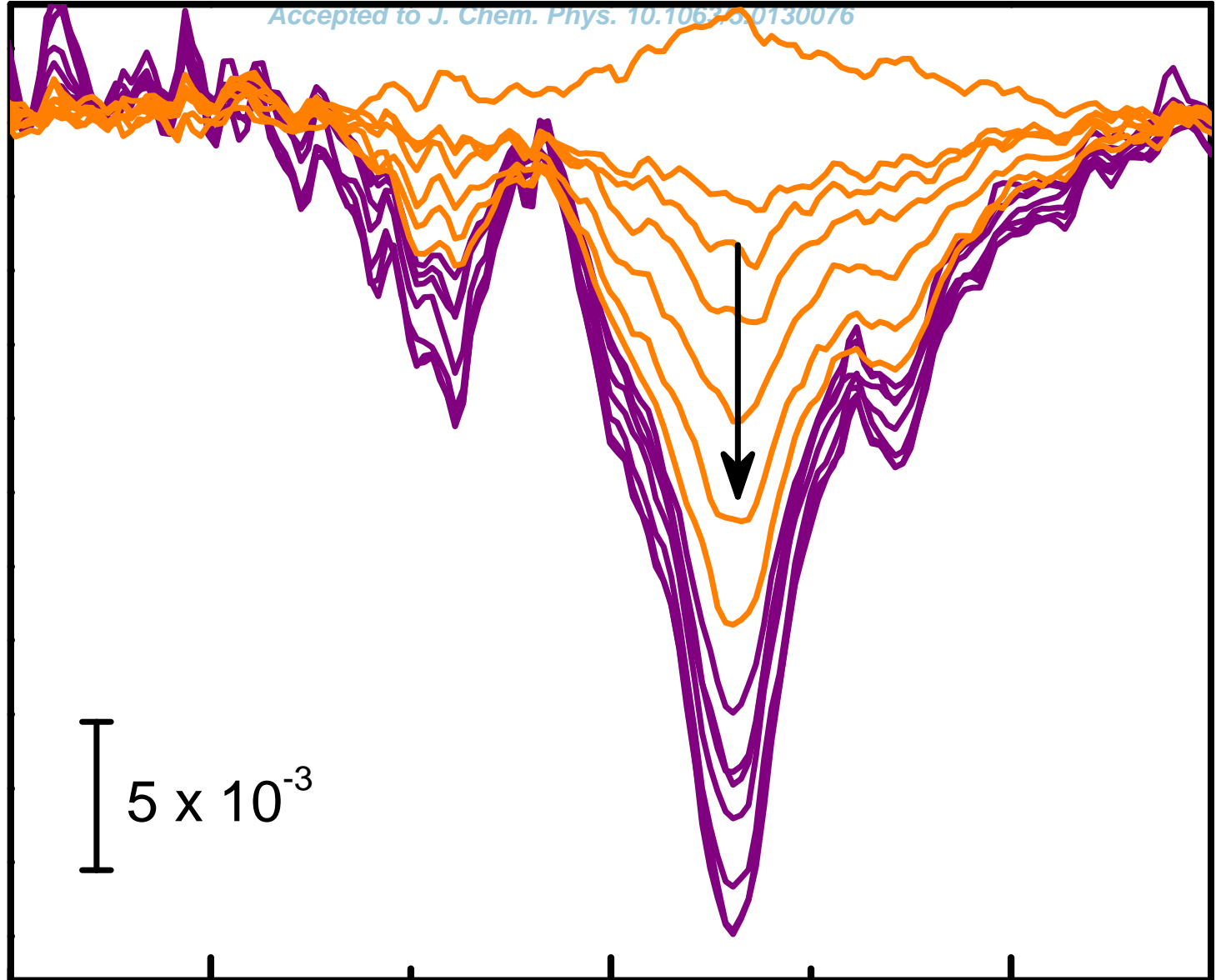
5×10^{-3}

1500

1400

1300

wavenumber / cm^{-1}



absorbance

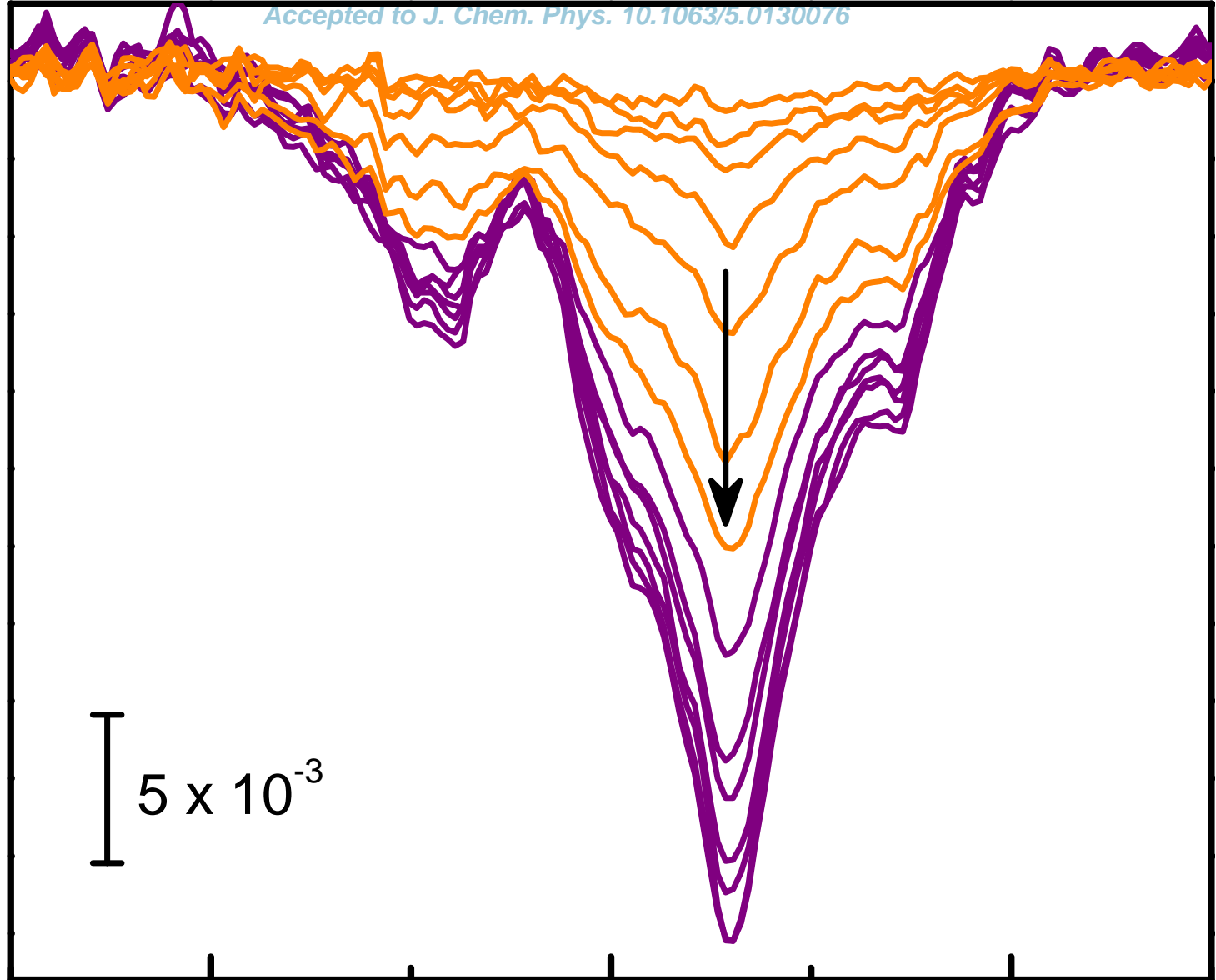
5×10^{-3}

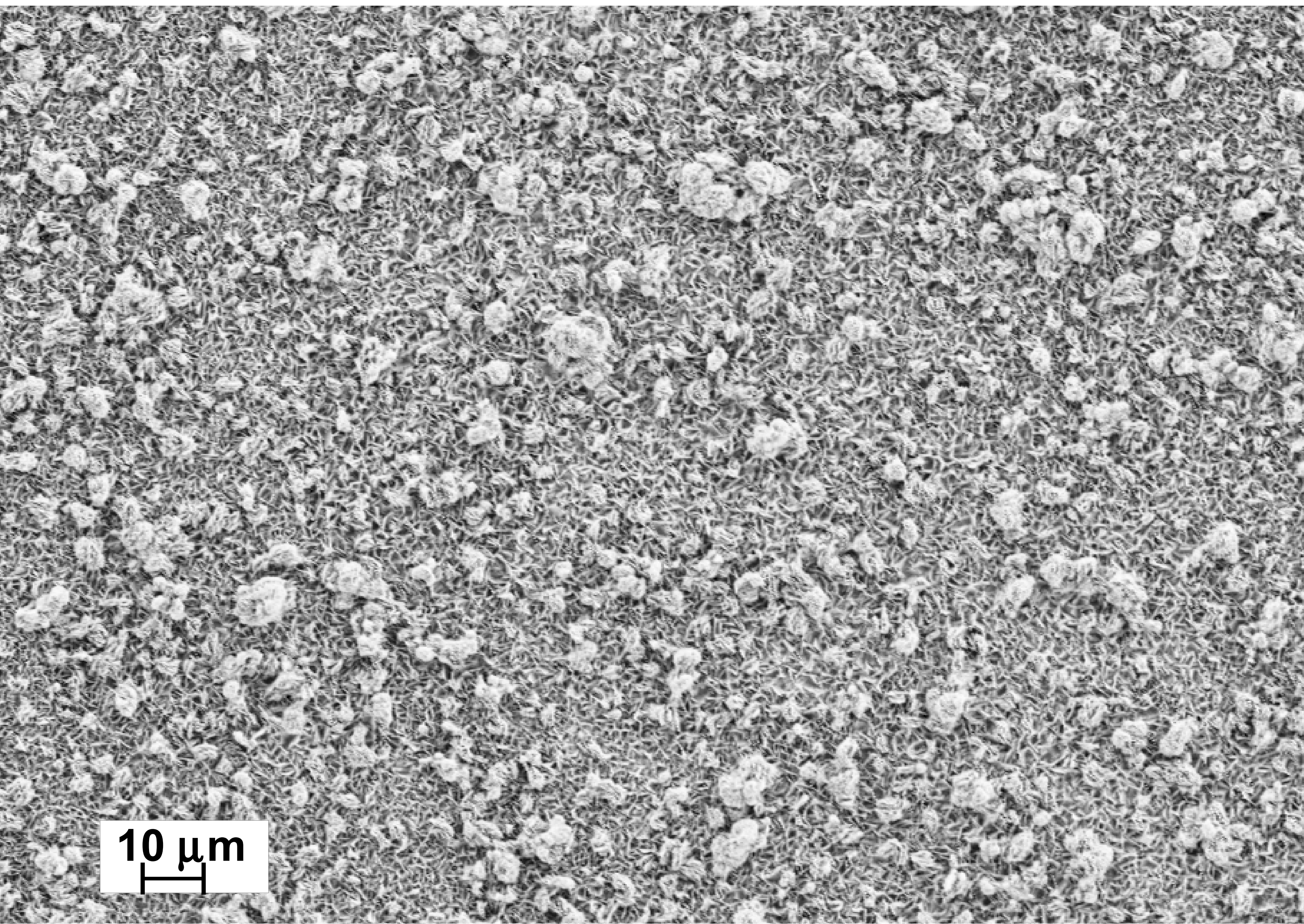
1500

1400

1300

wavenumber / cm^{-1}





10 μm

